

The Environments around Long-Duration Gamma-Ray Burst Progenitors

Christopher L. Fryer^{1,2}, Gabriel Rockefeller^{1,2}, and Patrick A. Young^{1,2}

ABSTRACT

Gamma-ray burst (GRB) afterglow observations have allowed us to significantly constrain the engines producing these energetic explosions. The redshift and position information provided by these afterglows have already allowed us to limit the progenitors of GRBs to only a few models. The afterglows may also provide another observation that can place further constraints on the GRB progenitor: measurements telling us about the environments surrounding GRBs. Current analyses of GRB afterglows suggest that roughly half of long-duration gamma-ray bursts occur in surroundings with density profiles that are uniform. We study the constraints placed by this observation on both the classic “collapsar” massive star progenitor and its relative, the “helium-merger” progenitor. We study several aspects of wind mass-loss and find that our modifications to the standard Wolf-Rayet mass-loss paradigm are not sufficient to produce constant density profiles. Although this does not rule out the standard “collapsar” progenitor, it does suggest a deficiency with this model. We then focus on the He-merger models and find that such progenitors can fit this particular constraint well. We show how detailed observations can not only determine the correct progenitor for GRBs, but also allow us to study binary evolution physics.

Subject headings: binaries: close—black hole physics—gamma rays: bursts—stars: neutron

1. Introduction

Since the concurrent and cospatial observation of supernova 1998bw with gamma-ray burst 980425 (Galama et al. 1998), evidence that long-duration gamma-ray bursts (GRBs) arise from the explosion of massive stars has continued to grow. This supporting evidence

¹Department of Physics, The University of Arizona, Tucson, AZ 85721

²Theoretical Division, LANL, Los Alamos, NM 87545

includes the association of long-duration GRBs with star-forming galaxies (Fruchter et al. 2002; Vreeswijk et al. 2001) and the detection of 1998bw-like “bumps” found in GRB afterglows (Bloom 2003). The connection between long-duration GRBs and massive stars was sealed by the paired observation of SN 2003dh and GRB 030329 (Hjorth et al. 2003; Stanek et al. 2003). This association tells us that the progenitors of long-duration GRBs are almost certainly massive stars. Both theory and observation further constrain the nature of these massive star GRB progenitors. A successful GRB engine must produce beamed jets of relativistic matter with Lorentz factors in excess of 100 (Frail et al. 2001). To reach and maintain the high Lorentz factors observed in GRB ejecta, the jet must not sweep up much mass and the jet engine must be active for the entire time during which the jet pushes through the star, leading theorists to argue that the massive star must lose its hydrogen mantle before exploding (Woosley 1993; Zhang, Woosley, & McFadyen 2003). Such a star would have been a Wolf-Rayet star before collapse and its resultant supernova explosion should have matched type Ib/c supernovae. Spectral observations of SN 2003dh have confirmed that the progenitor was a Wolf-Rayet progenitor (Hjorth et al. 2003; Stanek et al. 2003).

Wolf-Rayet stars are known to have strong winds with mass outflow rates beyond $10^{-5}M_{\odot}y^{-1}$ and wind velocities above $1000\text{km}s^{-1}$. Stellar winds sweep out the environment surrounding the star and, depending upon the density of the ambient medium, these wind-blown bubbles can extend beyond 10 pc (Dwarkadas 2005). The density profile for a free-streaming wind is simply determined by mass conservation: $\dot{M}_{\text{wind}} = 4\pi r^2 \dot{r} \rho(r) \rightarrow \rho(r) = \dot{M}_{\text{wind}} / 4\pi r^2 v_{\text{wind}} \propto r^{-2}$ where \dot{M}_{wind} is the mass loss rate of the wind (assumed to be constant) and ρ, v_{wind} are the density and velocity (or \dot{r}) of the wind respectively. The density profile takes on a r^{-2} radial dependence when we assume a constant wind velocity.

Very quickly, GRB fireball theorists (see Chevalier et al. 2004 for a review) realized that this density profile, with its characteristic $\rho \propto r^{-2}$ profile, would produce a different afterglow light curve than, for example, a constant density profile expected from alternate GRB models (e.g. the merger of a double neutron star system). With all of the evidence pushing toward massive star progenitors for long-duration GRBs, we would expect to find that GRB afterglows were better fit by $\rho \propto r^{-2}$ density profiles than by constant density profiles, but roughly half of all systems seem to be better fit by constant density profiles, with typical densities between 0.1 and 100cm^{-3} (Meszaros et al. 1998; Dai & Lu 1998; Chevalier & Li 1999; Panaitescu & Kumar 2002; Chevalier et al. 2004). The disagreement between our picture of massive star progenitors for GRBs and observations of the GRB afterglow remains an outstanding problem in our understanding of long-duration GRBs. In this paper, we will study predictions of the environments surrounding long-duration GRB progenitors in an effort to resolve the density-profile problem.

A number of different approaches might resolve this particular discrepancy. On one extreme, one can ignore the observations, hoping that future data will show a different trend and negate the current results¹. On the other extreme, one can rule out the current paradigm for long-duration gamma-ray bursts and search for a different, non-stellar progenitor. In between a number of options exist and we will pursue two of these: 1) our free-streaming $\rho \propto r^{-2}$ profile estimate for the density in the wind-blown region is an oversimplification; or 2) the progenitor does not reside in its wind-blown bubble when the GRB is produced. We further restrict our study to progenitors of the collapsar or collapsar-like GRB engine (Woosley 1993; Fryer & Woosley 1998; MacFadyen & Woosley 1999). This engine, which invokes the collapse of a massive star down to a black hole and the formation of an accretion disk around that black hole, only works for a small subset of massive star progenitors. We believe that by studying this small subset of progenitors, we may gain some insight into the environments surrounding GRB engines.

The first option, modifying the density profile in the wind-blown bubble, can be accomplished in a number of different ways and has already been studied at some level. Some observations can be made to fit a wind profile if the density is decreased (Wu et al. 2003; Dai & Wu 2003). Chevalier et al. (2004) have also, in a generic sense, studied the true termination radius of the Wolf-Rayet wind. If the wind terminates at a small radius, the observations are probing the constant density region beyond the termination shock, and not the $\rho \propto r^{-2}$ free-streaming wind region. In §2 of this paper, we study the wind profiles of massive stars designed to produce collapsars (“massive star” progenitor to the collapsar engine), using a combination of stellar evolution models and 1-dimensional and 3-dimensional wind models. The wind mass loss is time-dependent, and we study the effects of this time dependence. Most working collapsar models require binary interactions, and we also study these binary effects.

Alternatively, there is a collapsar progenitor scenario where, before the GRB explosion, the progenitor moves out of its wind nebula: this is the helium-merger progenitor (Fryer & Woosley 1998; Zhang & Fryer 2001). In this progenitor, the more massive star in a binary collapses to form a neutron star or black hole, providing a kick to its binary system. Not until its companion evolves off the main sequence and causes the stars to merge is a burst produced. Although Fryer & Woosley (1998) already predicted that such a progenitor would

¹A number of assumptions go into the afterglow models needed to estimate the density profiles and it could well be that these assumptions are incorrect. Although roughly half of all explosions are better fit by a wind density profile ($\rho \propto r^{-2}$), constant density profiles can not be ruled out for any gamma-ray burst. But for Only 1 or 2 cases can a r^{-2} density profile be ruled out emphatically (Panaitescu - private communication). This observation is far from certain.

more likely yield a surrounding environment akin to a constant density interstellar medium (ISM) environment, no work to date has studied this claim in detail. In §3, we show results of Monte Carlo calculations to study the positions of these bursts relative to the formation site of their binary progenitor.

We ultimately find that the seeming discrepancy between simple wind models and GRB afterglow observations can play an important role in homing in on the true progenitor of these long-duration bursts. Although we can not rule out the massive star progenitor GRB scenario, it is becoming increasingly difficult to match such a progenitor to observations. The helium merger scenario is best able to fit current afterglow lightcurves, but it may have problems matching other observational constraints. We conclude by discussing the issues remaining for the different long-duration GRB scenarios.

2. Stellar Winds from Collapsar Progenitors

Weaver et al. (1977) first discussed the structure of wind-driven bubbles produced by massive stars. Assuming that the wind profile varies with at most a linear dependence on time and is spherically symmetric, the structure of these wind-blown bubbles is well known (Koo & McKee 1992a,1992b). However, as we shall see in this section, neither of these assumptions is strictly true. We study the bubble structure produced by the rapidly varying winds from Wolf-Rayet stars, the likely progenitor star for collapsar GRBs.

2.1. Understanding Wind Profiles

Before we study realistic wind profiles based on stellar mass-loss histories, we first build our intuition of bubbles from winds with constant mass-loss rates blowing into environments with different densities. Such wind blown bubbles have been studied in detail analytically (Koo & McKee 1992a,1992b; see Dwarkadas 2005 for a review) and the wind environment can be described by 4 separate regions: (1) the freely-flowing fast wind, (2) the shocked fast wind, (3) the shocked interstellar medium and (4) the unshocked interstellar medium. For the purpose of comparing to the afterglow observations, the primary constraints come from the first region, where the free-flowing winds develop a $\rho \propto r^{-2}$ density profile. To overcome the observational constraints, we must either lower the density of this region or limit its size. The free-flowing region is capped by a termination shock ($r_{\text{termination}}$), and we will focus on determining what conditions can drive down this termination shock to low radii: $r_{\text{termination}} < 0.1 \text{ pc}$. At such small size scales, the GRB jet can pass through this

region without seriously impacting the afterglow emission.

To understand the dependence of the termination shock radius on the uncertainties in wind parameters, we have modified the 1-D Lagrangian code developed by Fryer et al. (1999) to include the addition of mass from winds. Wind material is added in zones of constant mass. For constant mass loss from winds, this means that zones are added at constant time intervals. The inner boundary of the simulation moves out with the wind velocity. When a particle is added, its outer radius is set to the inner boundary radius and the inner boundary is set to the initial inner boundary radius. By varying the time intervals according to individual wind velocities, this technique can be used to simulate winds with varying mass loss rates and varying velocities. We model a region from ~ 0.01 to 20-200 pc. For our 1-dimensional, constant mass-loss studies, the interstellar medium is modeled with between $\sim 50,000$ and 100,000 zones. In 250,000 y, roughly 25,000 zones are added to the simulation. Table 1 summarizes all of the parameter study models.

Figure 1 (top) shows the density profiles for four different wind bubble simulations differing only in the density of the ambient medium (roughly 10, 100, 1000, and 10,000 cm^{-3}). We have assumed a constant wind velocity (1000 km s^{-1}) and constant mass loss rate ($10^{-5} M_{\odot} \text{ y}^{-1}$) which roughly corresponds to what we would expect from a Wolf-Rayet wind. A lot can be learned from these simulations, but we will focus on the radius of the termination shock ($r_{\text{termination}}$). 250,000 y of this strong wind produces a termination shock that is at a radius of 1 pc if the wind is blowing into an interstellar medium with a density of 100 cm^{-3} . Fitting to these simulations, we find that the radius of this termination shock is $\approx 1(n_{\text{ISM}}/100 \text{ cm}^{-3})^{-1/2} \text{ pc}$. It would require very high densities indeed to place the termination shock below 0.1 pc. We include a final simulation (dotted line) that includes a cooling routine outlined in Fryer et al. (2006) based on the cooling rates of Sutherland & Dopita (1993). The primary effect of cooling is to alter the density profile near the shock with the interstellar medium. Another effect is the fact that the UV photons from the star will drive an ionizing front ahead of the wind. This has been recently studied by van Marle et al. (2004). Although much more must be done to understand its effects, van Marle et al. (2004) found that the primary change from the ionization front was in the outer radius of the wind shock. It does not significantly alter the radius of the free-streaming region and we will not consider it further in this paper.

Figure 1 (bottom) shows the dependence of the termination shock radius on the other free parameters in a constant wind: the mass-loss rate (solid lines) and the wind velocity (dotted lines). Here we have assumed a low density interstellar medium (10 cm^{-3}). The dark solid line assumes a mass-loss rate of $10^{-4} M_{\odot} \text{ y}^{-1}$ whereas the light solid line assumes a mass-loss rate of $10^{-6} M_{\odot} \text{ y}^{-1}$. The termination shock radius is also proportional to the mass

loss to the $1/3$ power. The dark and light dotted lines assume wind velocities of 500 km s^{-1} and 2000 km s^{-1} respectively. Although this changes the position of the outer shock of the wind-blown bubble, it does not significantly affect the radius of the termination shock.

To restrict the termination shock to a radius below 0.1 pc , either the ambient density surrounding the GRB progenitor must be high ($n_{\text{ISM}} > 10,000 \text{ cm}^{-3}$) or the Wolf-Rayet wind must have a mass-loss rate much lower than the canonical $10^{-5} M_{\odot} \text{ y}^{-1}$. Such constraints may not be that extreme. Densities in excess of $10,000 \text{ cm}^{-3}$ are common in molecular clouds, especially near massive star birthsites. For example, the shock producing the young supernova remnant Cas A is impacting a $650 M_{\odot}$ molecular cloud with densities of 10^7 cm^{-3} . Unfortunately, such a dense medium is ruled out already by afterglow observations (Berger et al. 2003; Chevalier & Li 2000; Panaitescu & Kumar 2002; Kobayashi & Zhang 2003)².

However, the Wolf-Rayet mass-loss rate could be much lower than the canonical value for the specific stars that make GRB progenitors. Such a low mass-loss rate might result from a helium star formed in a binary interaction that causes a $15\text{-}20 M_{\odot}$ star to become a Wolf-Rayet star. Such a star can have a Wolf-Rayet mass loss rate as low as $10^{-7} M_{\odot} \text{ y}^{-1}$. This is not entirely satisfactory, as we believe such a star is not likely to collapse to a black hole. Alternatively, because the Wolf-Rayet mass-loss rate depends upon the metallicity ($\dot{M}_{\text{Wolf-Rayet}} \propto Z^{0.5} - Z^{0.9}$), GRB progenitors with observed surroundings matching constant density profiles could be limited to low metallicity stars (Yoon & Langer 2005). A low metallicity star turned Wolf-Rayet via a binary common envelope phase could have a very low Wolf-Rayet mass loss rate. For example, if $\dot{M}_{\text{Wolf-Rayet}} \propto (Z)^{0.9}$ (where Z is the metallicity), then a $25 M_{\odot}$ star with a metallicity $1/100$ th that of solar could have mass loss rates below $10^{-7} M_{\odot} \text{ y}^{-1}$. Not only will the free-streaming region of this wind be small, but its total density will also be low (a better fit to the observations). With such stars, ambient densities of a few hundred cm^{-3} would be sufficient to restrict the termination shock to less than 0.1 pc .

Before we move onto the complexities arising from realistic wind models, we mention a few other effects that may also limit the free-streaming wind profile in GRB progenitors. These stars may only form in very dense clusters and, if so, the interaction of the winds could limit the extent of the free-streaming profile. Rockefeller et al. (2005) studied the hydrodynamics of winds in the Arches and Quintuplet clusters. By analyzing their data, we find that the free-streaming wind region of even the strongest winds can be capped at 0.5 pc

²Although bear in mind that if we are observing the GRB shock as it progresses through shocked wind and ISM material, the observed density will be much less than the density of the interstellar medium. Thus, it is possible that large interstellar medium densities can exit.

at the center of the cluster.

In addition, these massive stars may have large velocities with respect to their circumstellar environments. The ram pressure of the wind environment against this circumstellar environment limits the extent of the wind. This extent can easily be derived by setting the free-streaming wind pressure $\equiv 0.5\rho_{\text{wind}}v_{\text{wind}}^2 = \dot{M}_{\text{wind}}/(8\pi)r_{\text{wind}}^{-2}v_{\text{wind}}$ to the ram pressure of the motion through the circumstellar medium $\equiv 0.5\rho_{\text{ISM}}v_{\text{star}}^2$. Here $\rho_{\text{wind}}, v_{\text{wind}}, r_{\text{wind}}$ and \dot{M}_{wind} are, respectively, the density, velocity and radial extent and mass-loss rate of the free-streaming wind; ρ_{ISM} is the density of the interstellar medium, and v_{star} is the motion of the star with respect to this circumstellar medium. Setting these two ram pressures equal, we derive an equation for the radial extent of the wind:

$$r_{\text{wind}} = 0.56 \left(\frac{\dot{M}_{\text{wind}}}{10^{-5}M_{\odot}\text{y}^{-1}} \right)^{0.5} \left(\frac{v_{\text{wind}}}{1000 \text{ kms}^{-1}} \right)^{0.5} \left(\frac{\rho_{\text{ISM}}}{10\text{cm}^{-3}} \right)^{-0.5} \left(\frac{v_{\text{star}}}{100 \text{ kms}^{-1}} \right)^{-1} \text{ pc.} \quad (1)$$

The number of massive stars with velocities in excess of 100 kms^{-1} is very low (10 – 30%: Hoogerwerf et al. 2001) and unless something in the progenitor evolution requires these fast velocities, it is unlikely that these motions can explain the environments.

2.2. Real Stellar Mass Loss

With the intuition gained from our constant mass-loss winds, we are set to attack the more realistic problem of stellar winds from GRB progenitors. In this paper, we use the output from the Tycho stellar evolution code (Young & Arnett 2005) and we study three different possible GRB progenitors: a $40 M_{\odot}$ single star, a $23 M_{\odot}$ binary system and a $16 M_{\odot}$ binary system. In the binary systems, we assume that a common envelope phase removes the hydrogen envelope of the primary when the primary star expands off the main-sequence. The mass loss rate and wind velocities for the GRB progenitors are calculated at each timestep during the evolution. Three prescriptions are used during steady mass loss phases. Mass loss for blue, hydrogen-rich stars ($\log T_{\text{eff}} > 3.875$) uses Kudritzki et al. (1989). At lower effective temperatures appropriate for the red giant/supergiant phases, the prescription of Bloeker (1995) is used. For Wolf-Rayet mass-loss rates, we use the Lamers & Nugis (2003) prescription.

Catastrophic mass loss episodes are dealt with in a more schematic fashion. The $40 M_{\odot}$ star is subject to luminous blue variable eruptions. The conditions for the instability (large radiative accelerations at temperatures coinciding with “bumps” in the continuum opacity) are identifiable in the stellar model. When these conditions are satisfied a large amount of mass is removed from the model to mimic an eruption. Limitations on the numerical stability

of the code prevent the mass from being removed as quickly as in a real luminous blue variable (LBV) eruption. Instead mass is lost at a high but steady rate dictated by code stability for a period of order 100 years with exact duration dictated by the amount of mass loss necessary. Such episodes can be identified in Figure 2. We choose a conservative approach, removing only enough mass to stabilize the stellar structure, though it is possible that the envelope could be removed to the depth of the instability generating region. Depending on the stellar structure, this could represent several solar masses of ejection. In the first, large eruption $\sim 1M_{\odot}$ is removed. Subsequent eruptions are smaller, and the bulk of the mass loss occurs via steady winds.

The 16 and 20 M_{\odot} models are intended to represent stars which lose their hydrogen envelopes during the first ascent Red Giant Branch (RGB) to a binary interaction. As with catastrophic eruptions, the physical processes cannot be captured realistically in a 1D stellar evolution code, so we must use an approximation. A similar procedure is used, which results in an ejection of the hydrogen-rich envelope ($\sim 10 M_{\odot}$, depending on stellar mass and mass loss history) in less than a thousand years. From an evolutionary standpoint, this is a good approximation, as the nuclear timescale of the star is much greater than a thousand years at this stage. This is not necessarily a good approximation to the mass loss, but it does provide the correct qualitative behavior: a short period of very high density, low velocity ($\sim v_{escape}$) mass loss which clears a cavity around the star into which a fast Wolf-Rayet type wind expands. The star subsequently evolves as a WR towards a Type Ib supernova. Though the binary ejection of the hydrogen envelope is handled only in a very schematic way it does represent, along with the subsequent evolution, a significant improvement over constant density or power law density profiles for the circumstellar medium.

The Wolf-Rayet mass loss is characterized by a high mass loss rate, high velocities, and an episodic history. The abrupt changes in mass loss occur when the main driver for the mass loss switches between opacity bumps at different temperatures and hence different radii in the star (see Lamers & Nugis 2003 for a discussion of the Wolf-Rayet mass loss mechanism). Early transient spikes may represent eruptions driven by high radiative accelerations in the stellar atmosphere akin to LBV or Ofpe (Massey et al. 2000) eruptions.

2.3. Wind-Blown Bubbles From Real Winds

The winds from our Tycho models have a number of characteristics that will complicate the wind profile. Note that the ejection velocity is often low when the mass loss peaks (either from a LBV eruption or a common envelop mass ejection). The high-velocity wind ejecta that follows these peaks will bounce against the slow-moving, dense, peak ejecta, causing a

shock to flow back down through the wind. Also, a similar shock will be produced when the eruption hits the termination shock. With realistic winds, our free-streaming, “unshocked” wind region now has many shocks running through it. This will dramatically affect the entropy profile of this wind. But afterglow observations are not sensitive to the entropy, but rather the the density profile of the wind-blown bubble region.

To study the density profile, we first return to our 1-dimensional simulations. By allowing non-constant time intervals for the addition of zones, we can incorporate the variable mass-loss rate and time-dependent wind velocity profiles from our Tycho models. We assume an ambient interstellar density of 100cm^{-3} . Table 1 lists the simulations of these realistic mass-loss profiles; we give rough ranges for the mass loss rates and velocities instead of absolute values. We model the wind-driven bubble only during the last few hundred thousand years of the star’s life: 0.6, 0.5, 0.6 Myr for the 16,23,40 M_{\odot} stars respectively. Although this reduced time does not accurately model the outer extent of the winds, it does get the position of the free-streaming region fairly accurately³. Most of the explosive phases of mass loss occurs during this time, and it is this ejecta that dominates the density profile of the free-streaming wind region. Figure 3 shows the density profiles of these models flowing in an ambient density of 100cm^{-3} . For these models, it is difficult to pinpoint the termination shock of the free-streaming wind and there is no strict $\rho \propto r^{-2}$ dependence to the density. But the density does decrease roughly as r^{-2} well beyond 1 pc. Recall that the termination shock from our $10^{-5} M_{\odot} y^{-1}, n_{\text{ISM}} = 100\text{cm}^{-3}$ calculation was at 1 pc (even for the 40 M_{\odot} star where the mass loss exceeds this standard value). The ambient medium would have to exceed 10^4cm^{-3} to reduce this region below 0.1 pc. This density is probably ruled out by the timescale of the radio emission (see Section 2.1).

We find that episodic spikes in the mass loss produce a termination shock which causes a significant departure from an $\rho \propto r^{-2}$ density profile. This does not help the situation much because the region of departure from a free-streaming profile propagates out from the star at roughly the velocity of the slow moving ejecta (\sim a few 100km s^{-1}). Thus the density profile is disturbed within the 0.1 pc limit for 1000 years or less, roughly 1% of the time between eruptions. Although we cannot rule out such episodes within 1000 years of collapse unless the stellar surface is hotter than $\sim 5 \times 10^5 K$ (hotter than the continuum opacity bumps which drive the high mass loss rates), the odds of an ejection event occurring within 1000 years of collapse are too small to explain the distribution of afterglows unless the frequency of ejection events increases as the star approaches collapse. We do not observe this behavior,

³Vikram Dwarkadas is currently modeling the full wind profiles of our binary star in an effort to understand the supernova remnant Cassiopeia A. The extent of the free-streaming region from his shock agrees with ours at the 20% level.

but the uncertainties in the physics of mass loss do not allow us to eliminate the possibility.

Another wrinkle in this model is the fact that these winds are far from spherically symmetric. As argued by Fryer et al. (1998), the idea that GRB progenitors most likely arise from binary systems is gaining increasing acceptance (Petrovic et al. 2005, Fryer & Heger 2005). If the wind is not already asymmetric due to rotation (Maeder & Meynet 2000), the binary interaction will ensure that it is. If the mass ejection arises from common envelope evolution, then this mass outflow at least is highly asymmetric. LBV eruptions are also observed to be strongly bipolar.

We have modified the three-dimensional SNSPH code (Fryer, Rockefeller & Warren 2005) to model these winds and then study the effects of asymmetries on the density structure. We add particles in shells centered on the location of the wind source, after a time $\Delta t \simeq h/v_{wind}$ has passed since the last addition of particles, where h is the SPH particle smoothing length and v_{wind} is the current value of the wind velocity. The mass of each particle is set according to $m = \dot{M}_{wind}\Delta t/n_{shell}$, where \dot{M}_{wind} is the current value of the wind mass loss rate and n_{shell} is the number of particles per shell. We remove particles from the simulation when they pass beyond 3 pc from the wind source.

Figure 4 shows the density profile of one such SPH simulation. A $23 M_{\odot}$ binary system, located at the center of the simulated volume, ejects material during a common envelope phase at a rate of $\sim 0.1 M_{\odot} \text{ yr}^{-1}$. We assume that this material is not ejected isotropically; instead, we place it in a 45° wedge oriented perpendicular to the z axis. The subsequent wind from the binary system has a much higher velocity but represents a much lower rate of mass loss from the system, so the wind collides with the inner edge of the dense wedge and flows out of the system primarily along the z axis. In this calculation, each added shell of wind material contains 400 SPH particles, each shell is added at a radius of 0.01 pc from the wind source, and the inner edge of the dense wedge is at $r = 0.3$ pc. The total number of particles in the simulated volume is $\sim 350,000$ but fluctuates slightly as the wind velocity changes.

Despite the modifications we have introduced to the wind profiles, we have not produced any conditions that cause the density profile of the wind-blown bubble to differ significantly from the $\rho \propto r^{-2}$ dependence. With these results in mind, our proposed solution for a the massive star progenitor for GRBs is a low-metallicity, 20-25 M_{\odot} star turned into a Wolf-Rayet star through a binary common envelope phase. A $23 M_{\odot}$ progenitor with a metallicity 1/100th that of solar would have a weak Wolf-Rayet wind, but also be massive enough to collapse to form a black hole. A GRB in a high metallicity host would rule out such a scenario, forcing us to progenitor models like the He-merger scenario.

3. He-Merger GRB Progenitors

Before we study the environments surrounding He-merger GRB progenitors, we first review the He-merger scenario itself. The He-merger progenitor for GRBs invokes a binary system where the most massive star collapses to either a neutron star or a black hole. If this compact object merges with its companion, it will spiral into the center of the companion while spinning up the companion. In this merger, the binary has satisfied the three main requirements behind the collapsar model: 1) the compact object accretes enough to collapse to a black hole, 2) the star surrounding the black hole has enough angular momentum (perhaps too much as we will discuss below) to form a disk around that black hole, and 3) the hydrogen envelope is ejected in a common envelope excretion disk.

There are two main binary evolution scenarios that dominate the production of He-Merger progenitors of GRBs: common envelope mergers and kick-induced mergers of nearly equal mass stars. Figure 5 shows the basic evolutionary phases in the common envelope scenario. In this scenario, we generally begin with an initial binary in a fairly close orbit ($\lesssim 1$ A.U.). The more massive star (“primary”) evolves off the main sequence and, for most progenitors, envelops its companion as it turns into a giant (or supergiant) star. This causes the orbital separation of the binary to tighten in a common envelope phase. The primary then collapses, forming either a neutron star or black hole. A fraction of these binary systems will remain bound after the supernova explosion. When the companion star evolves off the main sequence, it can envelop the compact remnant produced by the collapse of the primary. A fraction of these binaries will merge during this second common envelope phase, producing a helium-merger GRB.

The second main scenario we loosely term the “Brown” He-merger scenario because it uses similar initial conditions (a binary system with nearly equal massed stars) to a double neutron star formation scenario proposed by Bethe & Brown (1998). The idea of Bethe & Brown (1998) was to consider binary systems where the two stellar components have masses that are so close that the less massive star evolves off the main sequence before the more massive star collapses to form a compact remnant (this corresponds to masses of the two stars that are within $\sim 10\%$ of each other). In their model, the two helium stars produced during the mass transfer phase are pushed into a tight binary that remains bound through the two subsequent supernova explosions, forming a system with two compact objects. In our scenario, we follow the Bethe & Brown (1998) evolution up to the point that we form two helium stars in a tight binary (Fig. 6). When the first helium core collapses, its kick can drive it into its companion, producing a helium-merger GRB.

This “Brown” He-merger scenario uses supernova kicks to cause the compact object to merge with its stellar companion. This begs the question of whether a kick imparted to the

compact object formed during the collapse of the primary can drive the neutron star or black hole into its main sequence companion (Fig. 7). Because main sequence stars are not quite as compact as helium stars, we expect lower accretion rates in these models, possibly making this scenario less viable as a GRB progenitor. In addition, Fryer et al. (1999) pointed out that this main-sequence star mechanism is rare. We will explicitly discuss the rates here, finding that this mechanism accounts for less than $\sim 5\%$ of the total helium-merger GRB population for most simulations.

These three different progenitor scenarios produce very different environments through which the GRB jet will pass (Table 2). Both mechanisms 2 and 3 produce mergers very soon after (generally within a few years of) the supernova explosion. GRB explosions for these two scenarios will first pass through a young supernova remnant and then through the wind from the Wolf-Rayet progenitor. Scenario 1 does not produce a GRB until long after ($\sim 1 - 10$ Myr) the collapse of the primary star. With the kick imparted to the system during the collapse of the binary, most bursts from this progenitor occur beyond the edge of the supernova remnant and the Wolf-Rayet wind termination shock. Hence, the environment surrounding these bursts will not be the wind-swept structure characteristics we expect from Wolf-Rayet stars. The immediate environment surrounding these bursts will either be characterized by a constant density medium (if the companion is low-mass: $< 15 - 20 M_{\odot}$) or by the giant winds from the companion. In this section, we study the relative frequencies of occurrence of these different burst scenarios and their velocity, merger time, and position distributions including a brief study of the uncertainties of all these values.

3.1. Possible Constraints on the Helium merger

It is likely that only a subclass of He-mergers will produce GRBs. Currently we do not understand the progenitors or the collapsar mechanism well enough to definitively exclude some progenitors. Perhaps observations of GRBs can provide some insight into the progenitor subclass that truly makes GRBs. Here we discuss a variety of He-merger subclasses that may make up the true set of GRB progenitors. We will then study each of these subclasses separately when we present our population synthesis results. Table 3 summarizes these different subclasses.

One of the sources of uncertainty in our population synthesis studies is that we don't know exactly what conditions actually produce GRBs. For example, Fryer & Woosley (1998) assumed that the primary could collapse into either a neutron star or a black hole and still be a candidate GRB progenitor. Their assumption, which has been borne out by current simulations (Zhang & Fryer 2001), is that even if the compact remnant were a neutron star,

it would accrete so much in the inspiral phase that it would become a black hole quickly, satisfying the “black hole requirement” producing collapsars. But if the accretion rate is not so extreme (angular momentum, for example, could drive outflows), then the neutron star may not collapse to form a black hole and such a progenitor will not produce a collapsar. Alternatively, it may be that black holes accrete too much mass, making inefficient collapsars unable to drive strong GRB jets. We will look separately at systems whose primary collapses to a neutron star versus those systems whose primary collapses to form a black hole. This gives us two separate subclasses based on the initial status of the compact remnant: 1) a neutron star or 2) a black hole.

Another constraint on the progenitor may be the amount of angular momentum. When Zhang & Fryer (2001) modeled their mergers, they focused on maximizing the angular momentum surrounding their collapsar black hole. They assumed that the stars were, if anything, spinning in the same direction as the orbital angular momentum. They also assumed that very little orbital angular momentum was required to remove the hydrogen envelope and that all of the orbital angular momentum was deposited in the helium star. This produced very high angular momentum disks in the merged black hole accretion disk system, leading some to argue that this progenitor does not produce a viable GRB (Di Matteo et al. 2002). However, recall that Zhang & Fryer (2001) were trying to maximize the angular momentum in the system. The angular momentum could be much lower if most of the orbital angular momentum is lost to the hydrogen envelope or if the star is spinning in the opposite direction with respect to the binary orbit. Mergers produced with kicks may also lead to lower angular momenta. In general, we assume that a star’s spin direction in a binary coincides with the direction of the orbit. This is almost certainly true prior to the supernova explosion. But the kick imparted to the compact object during supernova explosion can (and often does for those binaries that remain bound) produce binaries where the spin angular momentum direction is 180 degrees off from the orbital angular momentum of the binary. This subclass is defined in our calculations by restricting our sample to those companion stars whose helium star moment of inertia (from the helium stars of Fryer & Heger 2005, $I_{\text{He-Star}} \approx 0.1 M_{\text{He-Star}} R_{\text{He-Star}}^2$) is greater than the moment of inertia of the merging compact object when it reaches the helium star radius ($I_{\text{CompactBinary}} = M_{\text{CompactObject}} R_{\text{He-Star}}^2$).

Lastly, if the companion star is too massive, it too will blow a wind, leading to a surrounding wind environment not too different from the Wolf-Rayet winds produced by the primary star. We define this subclass of low-mass losing systems by restricting our sample to systems with companions whose total mass-loss is less than $1 M_{\odot}$. This essentially limits us to binaries where the initial mass of the companion is less than $15 M_{\odot}$.

With these four subclasses in mind, we can now analyze our population synthesis studies.

3.2. Population Synthesis studies

Our population synthesis calculations are based on the code described in Fryer et al. (1998,1999). The main alteration to this code has been to update the mass of the collapsed core using the results of Fryer & Kalogera (2001). Fryer et al. (1999) set the remnant mass for stars collapsing to neutron stars to $1.4 M_{\odot}$ and the remnant mass for stars collapsing to black holes to one third the mass of the star at collapse. In this paper, we have fit a function to the results of Fryer & Kalogera (2001), allowing a more continuous spread of neutron star and black hole masses. We refer the reader to Fryer et al. (1998,1999) for any other details about the population synthesis technique or the specific code we use. We have run over a dozen models using a wide range of choices for the uncertain binary population synthesis parameters (Table 4).

Table 4 shows a list of all the population synthesis models studied in this paper followed by the values of the population synthesis parameters used by each model. For a more detailed description of each of these parameters, see Fryer et al. (1999). We focus on just a few parameters: the power law of the initial mass function (α_{IMF}), the distribution of velocities imparted to compact objects at collapse (kick), mass transfer parameters denoting the fraction of overflowing matter in a binary accreted by the companion (β_{MT}) and the specific angular momentum of the overflowing matter ejected, and hence lost, from the binary (α_{MT}), and the efficiency with which the inspiralling star in a common envelope phase ejects the envelope (α_{CE}). We sample both our primary and secondary stars from the same initial mass function, constraining the secondary to be less massive than the primary. After some argument about the distribution of kicks arising from stellar collapse, it is now generally accepted that a bimodal kick distribution like that proposed by Fryer, Burrows, & Benz (1998) is roughly correct (Arzoumanian et al. 2002). We term the kick distribution represented by two Maxwellians of 50 and 500 km s^{-1} the FBB kick distribution. We have also used a set of single Maxwellian distributions covering a range of mean values to better understand the of the dependence on the kick magnitude. Finally, we have run a few tests of the dependencies on the stellar mass loss rates and radii. We model 50 million binaries in each simulation.

Fryer et al. (1999) presented very few results outlining the characteristics of the Helium Merger model, focusing mostly on the formation rate. Here we study the distribution of merger velocities, merger times and distances traveled before GRB outburst for the various subclasses of He-merger progenitor. The explosion and the supernova kick impart a velocity to the binary (if it remains bound). Figure 8a shows the distribution of the post-collapse velocities of He-Mergers for our “Standard” model (Table 4). The dark solid line shows the number of binaries per 1 km s^{-1} bin for all He-merger progenitors. Although for most

subclasses, the bulk of the systems have velocities below 25 km s^{-1} (where the total number peaks), a second peak exists above 100 km s^{-1} . The two peaks arise because of the double peaked nature of the supernova kick distribution. The peak at low velocities is not present for two subclasses of He-merger models: those with initially black hole compact remnants and those with high moments of inertia. Note that the peak in low-velocity systems is dominated by the NS Collapse and Low-Wind models. Because the kick must nearly exactly counter the momentum lost in the supernova ejecta for our strong supernova models, the systems that are more likely to remain bound for these NS binaries are those where the countering effects lead to small proper motions. None of the kick velocities are high enough to escape their host galaxy’s gravitational potential unless the galaxy is extremely small.

Figure 8b shows the merger times for the same model as Fig. 8a. The peaks below 100 years arises from binaries following the “Brown Merger” scenario or the “MS Merger” scenario (Scenarios II and III)⁴. For most of these systems, the stars merge within a few months of the collapse of the primary. For Scenario I, the merger rates are determined by the remaining main-sequence lifetime of the companion. Note that the low wind (small mass) subclass dominates the long merger times, but nearly all of the subclasses have the full range of merger times. Figure 8c shows the distribution in distance traveled before outburst for the He-merger population. This distribution is determined by multiplying the velocity of the binary times its merger time. Here again, the $<1 \text{ pc}$ bin is made up entirely of the “Brown” scenario and the main-sequence kick scenario.

In Figures 8d-f, we show the same set of data for the velocity, merger time, and distance distributions as a function of fractions relative to the total number in a subclass instead of total number. Because the rate of these mergers is still very difficult to determine due to a number of uncertainties (e.g. binary mass fraction and initial mass function), such relative abundances are most appropriate for comparison to observations. From these plots we can see that in the total He-merger population, less than 20% occur within 1 pc of their initial formation site. This is essentially a statement that less than 20% of He-merger systems are formed in the Brown and MS Merger scenarios. The moment of inertia subclass produces the most extended distribution of mergers.

To demonstrate the effect of the kick distribution, we compare to a single Maxwellian kick distribution. Figure 9a-c shows the fractional distributions of velocity, merger time, and distance travelled for our Max300 mode. The scales have been kept identical to those used in figures 8d-f and these simulations can be compared directly. Note the lack of the

⁴The peak between 10-100y is produced by the Brown scenario in systems where the helium cores do not go through a common envelope phase but are kicked in such a manner to merger - very rare indeed

double peak in the velocity distribution. Figures 10 and 11 show the velocity, merger time, and distance travelled distributions for a series of models, but focusing only on the total He-merger population. Figure 10 focuses on different mass transfer and binary parameters - the two most important being stellar radii and stellar mass loss. Figure 11 shows the results of a series of models using single Maxwellian kick distributions of varying strengths.

Tables 5,6 and 7 summarize the results of all of the simulations. Table 5 shows the merger rates assuming that a massive binary is formed every 100y. In general, the standard He-merger scenario dominates $> 75\%$ of all the He-mergers formed. We confirm the results of Fryer et al. (1999) that the main sequence merger rate is very low ($< 5 - 10\%$ of all mergers). Given the high uncertainty in the rate, we can not rule out any scenario or subclass, or claim any subclass as the sole formation scenario or subclass based on the GRB rate, but both the main sequence merger scenario and the high moment of inertia subclass definitely have rates on the low end to be the sole path for GRB formation. Table 6 lists velocity and merger time information. High velocity systems are rare, so any observations that argue for a high velocity in the merging system would place strong constraints on some of the population synthesis uncertainties. The strongest constraint at the moment may well be the number of systems that merge within a wind background versus systems in a more constant medium. The effective observational constraint on this is the distance these systems travel before merging (Table 7). Systems with stars that initially collapse to form black holes tend to move faster but merge quicker, and are likely to be closer to their formation sites. As the observational implications get stronger, it is possible that we will be able to home in on the true GRB progenitor subclass.

Some final summarizing comments on the nature of these populations:

- Roughly 20% (15% if we exclude main-sequence mergers as they may not be dense enough to produce GRBs) of all He-mergers will occur with the wind-driven shroud produced by the collapse of the star forming the compact remnant for the GRB. These Bursts will not only occur within the wind, but also within a young supernova remnant (< 10 y old).
- The rest of the systems produce bursts ~ 1 -50 million years after the collapse of their massive component, roughly 10-100 million years after the initial burst of star formation.
- Although some bursts can occur 1 kpc away from their initial star formation, the bulk occur within 100 pc of their formation sites.

What do these results tell us about the environments around He-Merger GRBs? Although

the star forming the compact object in these systems may have had a Wolf-Rayet wind profile, because of the delay in the explosion, the environment surrounding the system during the GRB outburst need not have this r^{-2} density profile. If all of the progenitors we discussed here make GRBs, 80% of He-mergers will *not* be characterized by a strong Wolf-Rayet wind environment. If the companion to the compact remnant exhibits strong winds, its wind profile will dominate the surrounding medium. But, in our simulations, 60-90% of the companions have masses below $15\odot$ and hence will not have winds that strongly affect the surrounding medium. In comparing to GRB afterglows, the surrounding media of these systems ($80\% \times 60\text{-}90\% = 50\text{-}70\%$ of all systems) will exhibit constant density profiles. But take these fractions with some caution - we do not know what subset of all He-mergers will actually produce GRBs, and depending upon this subset, the relative rates will change.

4. Conclusion

We have studied the environments around collapsar-like long-duration gamma-ray bursts. We have focused on two classes of progenitors that have been proposed to explain these GRB explosions with their associated supernovae: the collapse of a massive star and the merger of a compact object with its stellar companion. The progenitor class leading to massive star collapse is characterized by progenitors whose mass loss prior to collapse is extremely high. The environment surrounding these progenitors is defined by this mass loss rate. The general assumption (e.g. Chevalier et al. 2004) is that the density profile follows an r^{-2} profile with a density proportional to a constant mass loss. But the mass loss for these massive stars is anything but constant. This variability leads to modifications to the r^{-2} profile. In addition, the mass loss can be significantly asymmetric, leading to additional wrinkles in the profile of the surrounding environment. In general, these modifications are not sufficient to resolve the discrepancies between predictions of this progenitor scenario and the observations. Recent work studying mass loss in GRB progenitors has indicated that these environment observations contain a wealth of information about the bursts (van Marle et al. 2005, Eldridge et al. 2006).

Although further study (both theoretical and observational) is required, we are now pushed to some extreme predictions in order for the classic massive star progenitor scenario for GRBs to produce roughly half of all GRB explosions within constant density environments. In addition, the low densities predicted by some GRB progenitors will be much harder to produce with massive star progenitors. This, in effect, is strike two for the massive star collapse progenitor for long-duration GRBs – the first strike being the difficulty in getting enough angular momentum to form black hole accretion disks in these progenitors

(e.g. Petrovic et al. 2005, Fryer & Heger 2005). A possible solution may still exist if GRB progenitors are low-mass ($20\text{-}25 M_{\odot}$), low-metallicity stars. The resultant Wolf-Rayet winds for such stars could be less than $10^{-7} M_{\odot} y^{-1}$.

The other class of progenitor, the He-merger model, invokes the merger of a compact remnant from a massive star with its companion. Although this progenitor model also begins with a massive star with strong winds, the system can travel up to 1 kpc from this wind environment prior to the GRB explosion. We described 3 different formation scenarios: the classic ‘‘He-merger’’ model produced when the companion envelops its compact remnant companion, the Brown merger scenario requiring nearly equal-massed binary stars, and the main-sequence kick scenario. The relative rates of these three scenarios are roughly 80:15:5 respectively. Essentially all of the classic He-merger systems explode more than 10 pc from their initial formation site. For these models, the surrounding environments are not set by any wind profile (unless the companion star also has a strong wind). In contrast, the Brown and main-sequence merger scenarios occur within the wind profile of the compact remnant forming star. Indeed, the GRB from these scenarios will occur within 10-100 y of the collapse of the primary (and its possible explosion). Assuming that these scenarios produce all long-duration GRBs, we predict at least 20% of all GRBs should have wind profiles. The remaining 80% will exhibit weaker wind environments (not from Wolf-Rayet stars) of the NS/BH companion, 60-90% of which are stars with masses below $15 M_{\odot}$. This means that, if all He-mergers produce GRBs, we expect that 50-70% of all GRBs should occur in ISM-like surroundings. Roughly 20-30% of these bursts will occur more than 100 pc from their initial formation sites.

It appears that the He-merger class of long-duration progenitors fits the constant density surroundings better than the stellar collapse progenitors. This is not surprising. Fryer & Woosley (1998) proposed this model, in part, to explain this observation. However, this model still has one strike against it: these mergers tend to have too much angular momentum. Note also that these progenitors predict significant hydrogen in an excretion disk not too far from the collapsing star. Although one would not expect hydrogen lines to be strong in the supernova explosion accompanying the GRB from this He-merger progenitor, ultimately evidence of the supernova shock interacting this disk may produce some hydrogen emission akin to the hydrogen line emission observed in the Type Ia supernova 1999ee (Mazzali et al. 2005).

If He-mergers are the only long-duration GRB progenitor, these constraints will probably require that only a subset of all the possible He-merger models actually produce GRBs, but much more detailed calculations (both of population synthesis and of common envelope mergers) are required to constrain this subset. Observations combined with population

synthesis studies may provide clues to the true subclass of He-mergers responsible for the formation of GRBs.

If observations can constrain the subclass of He-mergers that produce GRBs, we may also be able to constrain some of the uncertainties currently plaguing population synthesis calculations. We can use these comparisons to help validate our population synthesis codes for use in other binary calculations: e.g. the prediction of populations of X-ray binaries. These calculations also ultimately teach us about stellar evolution. The most clear-cut examples of uncertain parameters in this study are stellar radii and stellar winds. In this way, studying the environments around GRBs not only teach us about GRBs, but also the objects that make GRBs.

Alternatively, both progenitor scenarios may produce GRBs: the He-merger model would be responsible for producing all $\rho = \text{constant}$ ambient medium bursts along with some of the $\rho \propto r^{-2}$ bursts; the classic massive star progenitor will account for a fraction of the $\rho \propto r^{-2}$ wind-blown bubble bursts.

Acknowledgments This work was funded in part under the auspices of the U.S. Dept. of Energy, and supported by its contract W-7405-ENG-36 to Los Alamos National Laboratory, by a DOE SciDAC grant DE-FC02-01ER41176 and NASA Grant N5-SWIFT05-0014.

REFERENCES

- Arzoumanian, Z., Chernoff, D.F., Cordes, J.M. ApJ, 568, 289
- Berger, E., Kulkarni, S.R., & Chevalier, R.A. 2002, ApJ, 577, L5
- Bethe, H., & Brown, G. E. 1998, ApJ, 506, 780
- Blöcker, T. 1995, A&A, 297, 727
- Bloom, J.S., Proceedings of “Gamma Ray Bursts in the Afterglow Era, Third Workshop” (Rome, Sept 2002), astro-ph/0303478
- Chevalier, R.A., & Li, Z.-Y. 1999, ApJ, 520, L29
- Chevalier, R.A., & Li, Z.-Y. 2000, ApJ, 536, 195
- Chevalier, R.A., Li, Z.-Y., & Fransson, C., ApJ, 606, 369
- Dai, Z.G., & Lu, T. 1998, MNRAS, 298, 87
- Dai, Z.G., & Wu, X.F. 2003, ApJ, 591, L21
- Di Matteo, T., Perna, R., & Narayan, R. 2002, ApJ, 579, 706
- Dwarkadas, V.V. 2005, ApJ, 630, 892
- Eldridge, J.J., Genet, F., Daigne, F., & Mochkovitch, R. 2006, MNRAS, 367, 186
- Frail, D.A. et al. 2001, ApJ, 562, L55
- Fruchter, A.S., et al. 1999, ApJ, 519, L13
- Fryer, C.L., Burrows, A., & Benz, W. 1998, ApJ, 496, 333
- Fryer, C.L., & Woosley, S.E. 1998, ApJ, 502, L9
- Fryer, C.L., Woosley, S.E., Hartmann, D.H. 1999, ApJ, 526, 152
- Fryer, C.L. & Kalogera, V. 2001, ApJ, 554, 548
- Fryer, C.L. & Heger, A. 2005, ApJ, 623, 302
- Fryer, C.L., Rockefeller, G., Hungerford, A., & Melia, F. 2006, accepted by ApJ
- Fryer, C. L., Rockefeller, G., & Warren, M. S. 2005, ApJ, submitted

- Galama, T. J., et al. 1998, *Nature*, 395, 670
- Hoogerwerf, R., de Bruijne, J.H.J., & de Zeeuw, P.T. 2001, *A&A*, 365, 49
- Hjorth, J., et al. 2003, *Nature*, 423, 847
- Kobayashi, S. & Zhang, B. 2003, *ApJ*, 582, L75
- Kudritzki, R. P., Pauldrach, A., Puls, J., & Abbott, D. C. 1989, *A&A*, 219, 205
- Lamers, H. J. G. L. M. & Nugis, T. 2003, *A&A*, 395L, 1
- Maeder, A., & Meynet, G. 2000, *ARA&A*, 38, 143
- MacFadyen, A.I. & Woosley, S.E. 1999, *ApJ*, 524, 262
- Massey, P., Waterhouse, E., & DeGioia-Eastwood, K. 2000, *AJ*, 119, 2214
- Mazzali, P.A., Benetti, S., Stehle, M., Branch, D., Deng, J., Maeda, K., Nomoto, K., Hamuy, M. 2005, *MNRAS*, 357, 200
- Mészáros, P., Rees, M.J., & Wijers, R.A.M.J. 1998, *ApJ*, 499, 301
- Panaitescu, A., & Kumar, P. 2002, *ApJ*, 571, 779
- Petrovic, J. Langer, N., Yoon, S.-C., & Heger, A. 2005, *A&A*, 435, 967
- Rockefeller, G., Fryer, C.L., Melia, F., & Wang, Q.D. 2005, *ApJ*, 623, 171
- Stanek, K. Z., et al. 2003, *ApJ*, 591, L17
- Sutherland, R. S. & Dopita, M. A. 1993, *ApJ*, 88, 253
- van Marle, A.J., Langer, N., Garcia-Segura, G. 2004, *RMxA&A*, 22, 136
- van Marle, A.J., Langer, N., Garcia-Segura, G. 2005, *A&A*, 444, 837
- Vreeswijk, P.M., et al. 2001, *ApJ*, 405, 273
- Woosley, S.A. 1993, *ApJ*, 405, 273
- Wu, X.F., Dai, A.G., Huang, Y.F., & Lu, T. 2003, *MNRAS*, 342, 1131
- Yoon, S.-C. & Langer, N. 2005, *A&A*, 443, 643
- Young, P.A. & Arnett, D. 2005, *ApJ*, 618, 908

Zhang, W., & Fryer, C.L. 2001, ApJ, 550, 357

Zhang, W., Woosley, S.E., & MacFadyen, A.I. 2003, ApJ, 586, 356

Table 1. Wind Parameter Study

Simulation Name	$N_{\text{zone}}^{0y} (N_{\text{zone}}^{0.25Myr})$ (10^4 zones)	\dot{M} ($M_{\odot}y^{-1}$)	n_{ISM} (cm^{-3})	v_{wind} (1000kms^{-1})	$r_{\text{termination}}$ ($r_{\text{termination}}$)	r_{outer} (r_{outer})
$\rho 10$	6.2(8.7)	10^{-5}	10	1	2.4	12.0
$\rho 100$	7.5(10.0)	10^{-5}	10^2	1	1.0	7.7
$\rho 100\text{cool}^{\text{a}}$	7.5(10.0)	10^{-5}	10^2	1	1.0	7.7
$\rho 1000$	9.3(11.8)	10^{-5}	10^3	1	0.42	5.1
$\rho 10000$	12.1(14.6)	10^{-5}	1.8×10^4	1	0.12	3.2
$\dot{M} \times 10$	6.2(8.7)	10^{-4}	10	1	4.8	18.4
$\dot{M}/10$	6.2(8.7)	10^{-6}	10	1	1.1	7.4
$v_{\text{wind}} \times 2$	6.2(8.7)	10^{-5}	10	2	2.0	16.0
$v_{\text{wind}}/2$	6.2(8.7)	10^{-5}	10	2	2.0	13.1
$16 M_{\odot}$	2.3(2.4)	$10^{-7} - 10^{-5}$	100	2-3	$\sim 45^{\text{b}}$	N/A
$23 M_{\odot}$	2.3(5.0)	$10^{-7} - 10^{-1}$	100	0.2-3.5	$\sim 2^{\text{b}}$	N/A
$40 M_{\odot}$	2.3(2.8)	$10^{-6} - 10^{-1}$	100	0.3-4.0	$\sim 2^{\text{b}}$	N/A

^aThis simulation uses the cooling routine outlined in Fryer et al. (2006) based on the cooling rates of Sutherland & Dopita (1993).

^bThe termination shock is less well defined for these models. Instead we give the radius at which a roughly $\rho \propto r^{-2}$ density profile ends. There is certainly structure within this radius, but probably not a sufficient deviation to change the conclusions of the afterglow constraints.

Table 2. Merger Scenarios

Name	Merger Mechanism ^a	Companion ^b	Merger Time ^c	Distance ^d
He-Merger ^e	CE	Evolved	$10^6 - 10^7$ y	$\sim 10 - \sim 1000$ pc
Brown Merger ^f	Kick	Evolved	< 100 y	< 0.1 pc
MS Merger ^f	Kick	Main-Sequence	< 100 y	< 0.1 pc

^aThe NS/BH merges with its companion either by being kicked into it during the supernova explosion (Kick) or by merging when the secondary expands off the main-sequence surrounding the NS/BH in a common envelope (CE).

^bWe differentiate the companion based on whether it has an evolved helium core or the unevolved core of a main-sequence star. The density in the evolved helium core can be much higher than that of a main-sequence star.

^cTime between the collapse of the primary (forming the compact remnant) and the merger of this compact remnant with the companion star.

^dDistance traveled by the system after the primary collapse.

^eFryer & Woosley (1998)

^fFryer et al. (1999)

Table 3. Subclasses

Name	Constraint	Trend in Progenitors
NS Collapse	$M_{\text{Primary}} > 20M_{\odot}$	Low-Mass Primary
BH Collapse	$M_{\text{Primary}} < 20M_{\odot}$	High-Mass Primary
Low-Wind	$M_{\text{Secondary}} < 15M_{\odot}$	Low-Mass Secondary
Angular Momentum	$I_{\text{HeStar}} > I_{\text{CompactBinary}}$	High-Mass Secondary

Table 4. Simulation Properties

Simulation	$\alpha_{\text{IMF}}^{\text{a}}$	$v_{\text{kick}}^{\text{b}}$	$\alpha_{\text{MT}}, \beta_{\text{MT}}^{\text{c}}$	$\alpha_{\text{CE}}^{\text{d}}$	Other
Standard	2.35	FBB	1.0,0.8	0.5	
StanCE0.5	2.35	FBB	0.5,0.5	0.5	
StanCE1.0	2.35	FBB	0.5,0.5	1.0	
StanCE0.2	2.35	FBB	0.5,0.5	0.2	
IMF2.7	2.7	FBB	1.0,0.8	0.5	
IMF2.7CE0.5	2.7	FBB	0.5,0.5	0.5	
IMF2.7CE1.0	2.7	FBB	0.5,0.5	1.0	
IMF2.7CE0.2	2.7	FBB	0.5,0.5	0.2	
IMF2.7MT1.0	2.7	FBB	NA,1.0	0.5	
FBBHighWind	2.7	FBB	NA,1.0	0.5	$\dot{M}_{\text{Wind}} = 10 \times \dot{M}_{\text{Wind}}^{\text{Stan}}$
FBBLowRad	2.7	FBB	NA,1.0	0.5	$R_{\text{Star}} = 0.1 \times R_{\text{Star}}^{\text{Stan}}$
FBBHighRad	2.7	FBB	NA,1.0	0.5	$R_{\text{Star}} = 4 \times R_{\text{Star}}^{\text{Stan}}$
Max50	2.7	50	0.5,0.5	0.5	
Max100	2.7	100	0.5,0.5	0.5	
Max150	2.7	150	0.5,0.5	0.5	
Max200	2.7	200	0.5,0.5	0.5	
Max300	2.7	300	0.5,0.5	0.5	
Max400	2.7	400	0.5,0.5	0.5	
Max500	2.7	500	0.5,0.5	0.5	
Max300IMF	2.35	300	0.5,0.5	0.5	
MaxHighWind	2.7	300	NA,1.0	0.5	$\dot{M}_{\text{Wind}} = 10 \times \dot{M}_{\text{Wind}}^{\text{Stan}}$

^aFor our models, we sample both the primary and the secondary from an initial mass function. We set the minimum primary mass to $9 M_{\odot}$. The secondary is allowed to be as low as $1 M_{\odot}$ and we insure that its mass is less than the primary.

^bWe use two kick distributions: a bimodal Maxwellian with mean velocities at 50 and 500 km s^{-1} based on the bimodal distribution from Fryer, Burrows, & Benz (1998) denoted FBB, and a single Maxwellian denoted by

the mean velocity.

^cMass transfer parameters: β_{MT} is the fraction of the expanding star’s envelope that is accreted onto the companion (the rest is assumed to be lost from the system), α_{MT} is the fraction of the specific angular momentum carried away by the mass that is lost. These parameters both determine the mass accreted by the companion and the orbital separation of the binary.

^dIf the expanding star envelops its companion, the companion will spiral in through the envelope. α_{CE} is a parameter designed to represent how efficiently the orbital energy ejects the envelope. It includes assumptions both about the binding energy of the expanding envelope and the amount of orbital energy injected during the inspiral. If this value is low, the final separation after a common envelope phase will also be small.

Table 5. Merger Rates (Myr^{-1})

Simulation	Formation Scenario					Subclass	
	Helium	Brown	MS	NS	BH	Low-Wind	Ang. Mom.
Standard	150	26	7	130	60	150	7.8
StanCE0.5	100	25	7.3	74	60	95	7.8
StanCE1.0	99	23	7.2	71	58	96	8.6
StanCE0.2	100	28	7.2	77	59	91	5.6
IMF2.7	160	19	4.5	140	40	160	5.0
IMF2.7CE0.5	103	19	4.5	82	45	98	5.8
IMF2.7CE1.0	96	18	4.4	68	40	95	5.6
IMF2.7CE0.2	100	20	4.3	84	40	93	3.6
IMF2.7MT1.0	68	19	4.5	51	41	65	5.0
FBBHighWind	160	4.3	0	149	12	149	0.24
FBBLowRad	2.7	38	0	21	20	6.6	1.1
FBBHighRad	110	5.4	19	100	35	120	4.4
Max50	0.13	0.026	0.0064	0.11	0.056	0.13	0.0066
Max100	120	30	7.5	96	65	120	8.1
Max150	72	22	6.7	52	49	69	6.3
Max200	46	16	5.4	32	36	44	4.7
Max300	18	7.9	3.0	12	17	17	2.4
Max400	5.7	3.5	1.3	3.4	7.1	5.1	1.1
Max500	1.5	1.4	0.46	0.78	2.5	1.3	0.38
Max300IMF	21	11	4.9	11	26	29	3.8
MaxHighWind	19	1.4	0.0	19	1.3	18	0.04

Table 6. Velocity and Merger Times

Simulation	Velocity $> 50\text{km s}^{-1}$ ($> 100\text{km s}^{-1}$) ^a				Mean Merger Time ^b ($1 - \sigma$ deviation)
	NS	BH	Low-Wind	Ang. Mom.	
Standard	0.31(0.04)	5.9(1.4)	5.0(0.47)	0.549(0.019)	9.9(5.6)
StanCE0.5	0.54(0.062)	4.1(0.53)	4.9(0.46)	0.83(0.030)	10.4(7.9)
StanCE1.0	0.54(0.065)	2.9(0.15)	4.4(0.41)	0.83(0.030)	10.6(8.1)
StanCE0.2	0.48(0.062)	7.7(1.7)	6.8(0.68)	0.82(0.033)	9.9(7.3)
IMF2.7	0.26(0.030)	5.3(1.1)	5.0(0.41)	0.36(0.011)	10.4(5.5)
IMF2.7CE0.5	0.46(0.056)	4.1(0.42)	5.4(0.39)	0.70(0.018)	11.0(7.9)
IMF2.7CE1.0	0.49(0.061)	2.7(0.12)	4.3(0.34)	0.61(0.016)	11.3(7.9)
IMF2.7CE0.2	0.42(0.055)	7.0(1.5)	6.6(0.60)	0.57(0.018)	10.4(7.1)
IMF2.7MT1.0	0.74(0.088)	3.0(0.13)	4.8(0.40)	0.87(0.024)	10.7(8.8)
FBBHighWind	0.077(0.0024)	0(0)	0(0)	0(0)	10.4(5.4)
FBBLowRad	24(14)	24(10)	12(2.0)	3.6(0.63)	9.5(9.9)
FBBHighRad	0.009(0)	2.4(0.096)	3.2(0.11)	0.25(0.0018)	10.1,4.8
Max50	0(0)	0.72(0)	3.0(0)	0.32(0)	11.1,(7.0)
Max100	0.42(0.0023)	2.3(0.0046)	2.9(0.0074)	0.56(0.0034)	11.0(8.1)
Max150	1.1(0.0054)	4.5(0.015)	5.6(0.015)	1.4(0.0015)	11.0(8.6)
Max200	3.1(0.016)	11(0.036)	13(0.043)	3.7(0.0041)	11.0(8.8)
Max300	11(0.10)	35(0.27)	40(0.21)	15(0.024)	11.0(9.2)
Max400	23(1.2)	49(1.7)	55(1.1)	24(0.19)	10.9(9.8)
Max500	44(9.6)	65(12)	69(7.8)	39(1.8)	11.0(10.7)
Max300IMF	13(0.13)	37(0.28)	41(0.22)	19(0.034)	10.1(9.3)
MaxHighWind	2.4(0.0052)	0.015(0)	0.54(0)	0(0)	10.4(5.4)

^aPercentage of systems in each subclass that have velocities greater than $> 50\text{km s}^{-1}$ ($> 100\text{km s}^{-1}$)

^bMean merger time in Myr ($1 - \sigma$ deviation in this merger time assuming Gaussian distribution).

Table 7. Distances Travelled between collapse and Merger

Simulation	Distances > 10 pc (> 100 pc) ^a			
	NS	BH	Low-Wind	Ang. Mom.
Standard	88(18)	53(22)	76(34)	91(21)
StanCE0.5	84(15)	53(23)	75(35)	90(22)
StanCE1.0	83(15)	58(24)	76(34)	90(23)
StanCE0.2	86(14)	44(17)	71(36)	89(19)
IMF2.7	89(18)	57(26)	77(38)	92(22)
IMF2.7CE0.5	85(16)	60(29)	79(42)	91(23)
IMF2.7CE1.0	84(16)	62(29)	68(39)	91(24)
IMF2.7CE0.2	87(15)	48(19)	73(40)	90(19)
IMF2.7MT1.0	82(13)	55(27)	76(91)	91(23)
FBBHighWind	90(19)	75(1.7)	28(2.4)	92(19)
FBBLowRad	0.54(0.20)	12(6.6)	92(52)	27(15)
FBBHighRad	84(6.6)	33(14)	35(18)	79(8.7)
Max50	87(17)	51(21)	58(24)	91(22)
Max100	84(18)	58(30)	79(43)	92(27)
Max150	79(17)	57(34)	77(49)	91(31)
Max200	76(15)	56(37)	77(52)	90(34)
Max300	69(15)	54(39)	75(56)	89(39)
Max400	57(13)	50(39)	74(60)	88(47)
Max500	36(8.4)	45(38)	76(66)	85(57)
Max300IMF	66(14)	50(34)	73(52)	87(40)
MaxHighWind	87(23)	79(2.3)	26(3.3)	93(24)

^aPercentage of systems in each subclass that have distances greater than > 10 pc (> 100 pc)

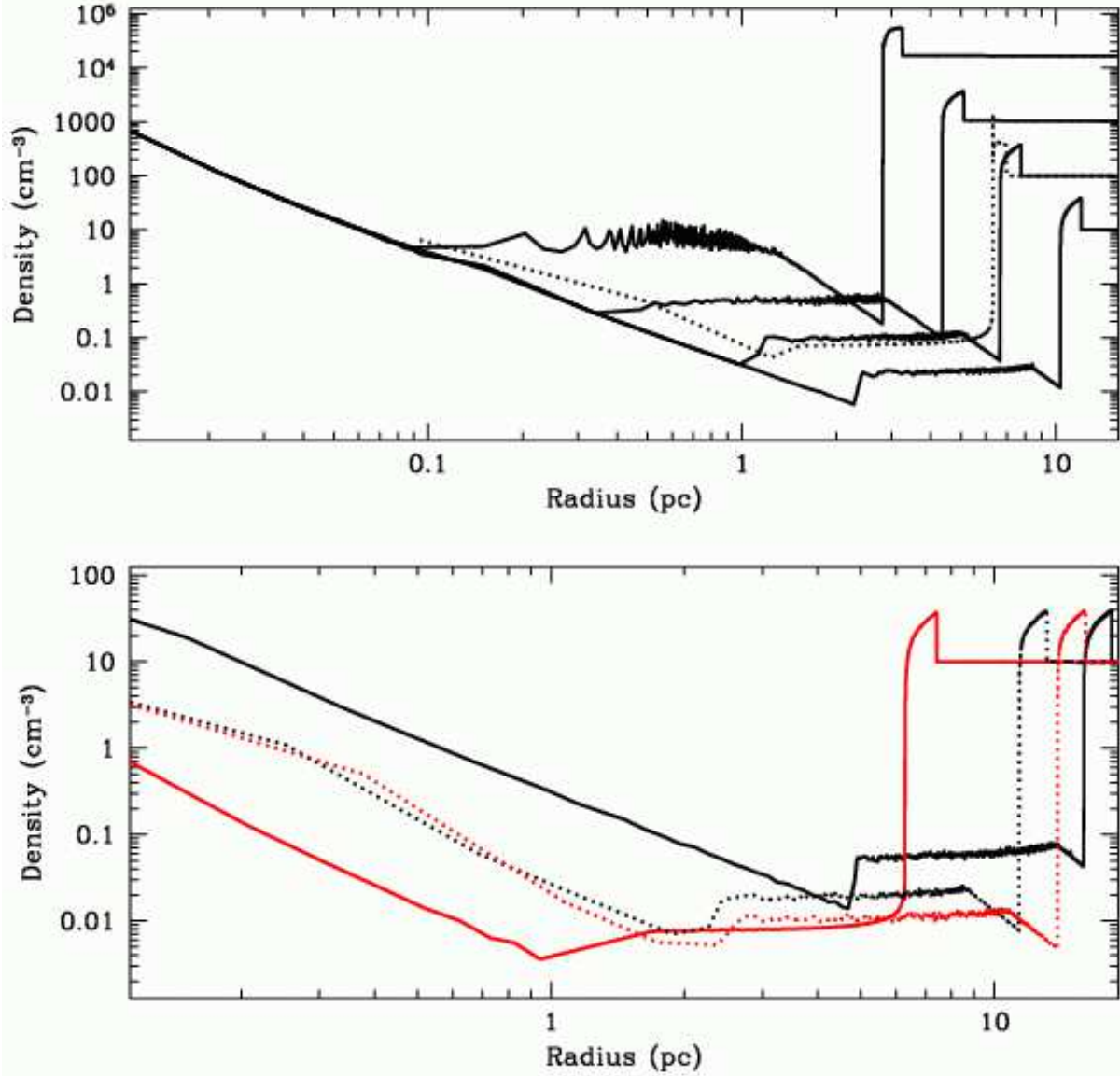


Fig. 1.— Density vs. radius for constant wind models. The top panel shows models with mass loss rates of $10^{-5} M_{\odot} y^{-1}$ and wind velocities of $1,000 \text{ km s}^{-1}$ for a range of densities in the ambient interstellar medium. The wind extends well into the interstellar medium (beyond 10 pc for ambient densities of 10 cm^{-3}). For afterglow observations, the most critical feature is the size of the free-streaming region. It is in this region that the density follows a $\rho \propto r^{-2}$ dependence on distance. This region is smaller for higher interstellar densities. Sound waves move back and forth through the shocked wind/ISM region, causing density perturbations, both real and numerical. The wiggles in the shocked region of our highest-density cases are numerical in origin. The dotted line in this top panel shows the result from our simulation including cooling (see Table 1 for details). The bottom panel studies the dependencies on the mass loss rate and the wind velocity around a model assuming a $10^{-5} M_{\odot} y^{-1}$ mass loss rate, wind velocity of $1,000 \text{ km s}^{-1}$ and ambient density of 10 cm^{-3} . The solid lines compare different mass loss rates: dark ($10^{-4} M_{\odot} y^{-1}$), light ($10^{-6} M_{\odot} y^{-1}$). The dotted lines

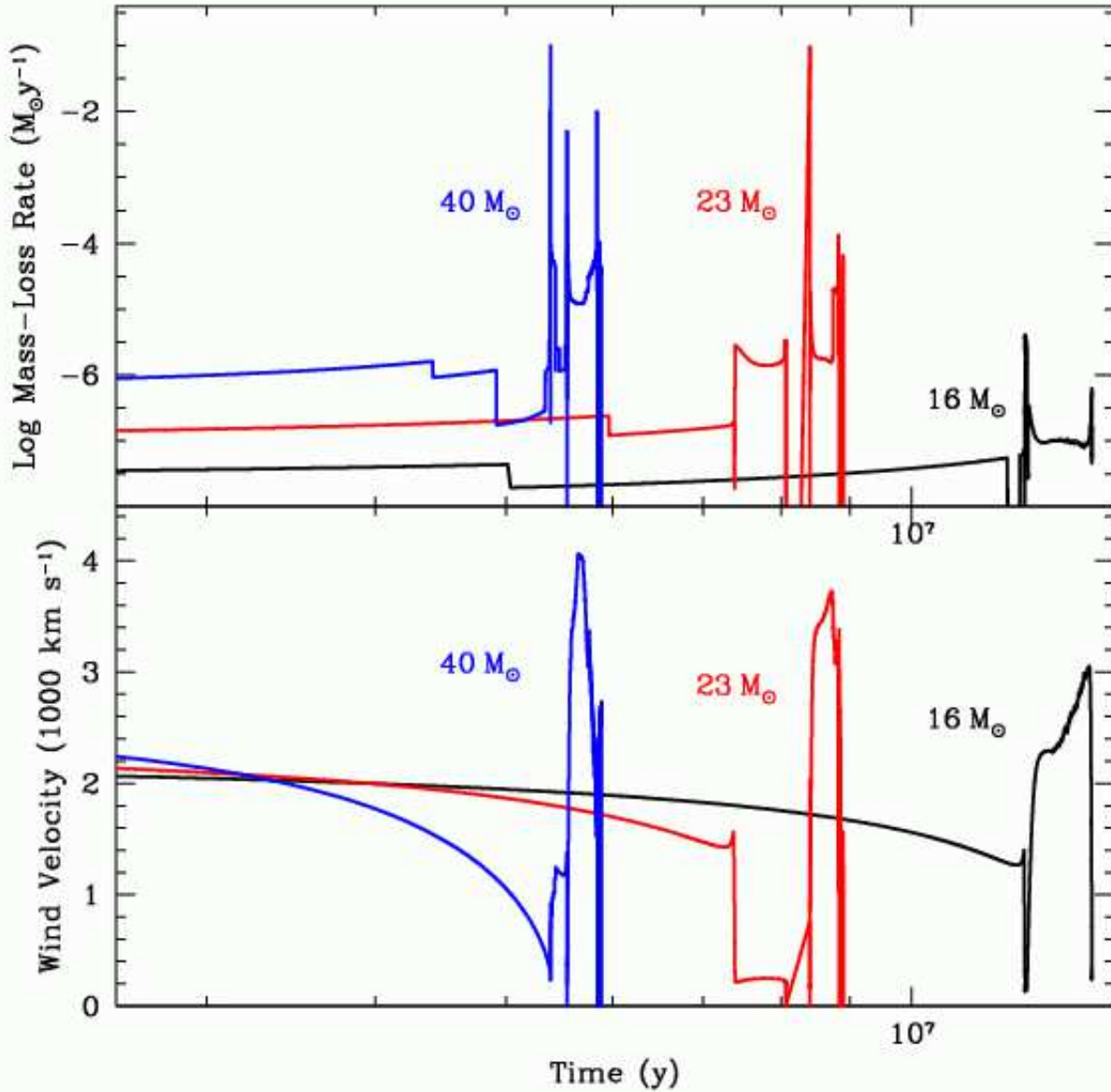


Fig. 2.— Mass loss rate (top) and wind velocity (bottom) time histories for three stellar models: 16 and 23 M_{\odot} binary systems and a 40 M_{\odot} single star. Note that the mass loss is far from constant with some pulses lasting for less than 100,000 y. The largest mass outflows often are the lowest velocity flows and this can lead to shocks as the fast moving material following the peak outflows catches these peaks.

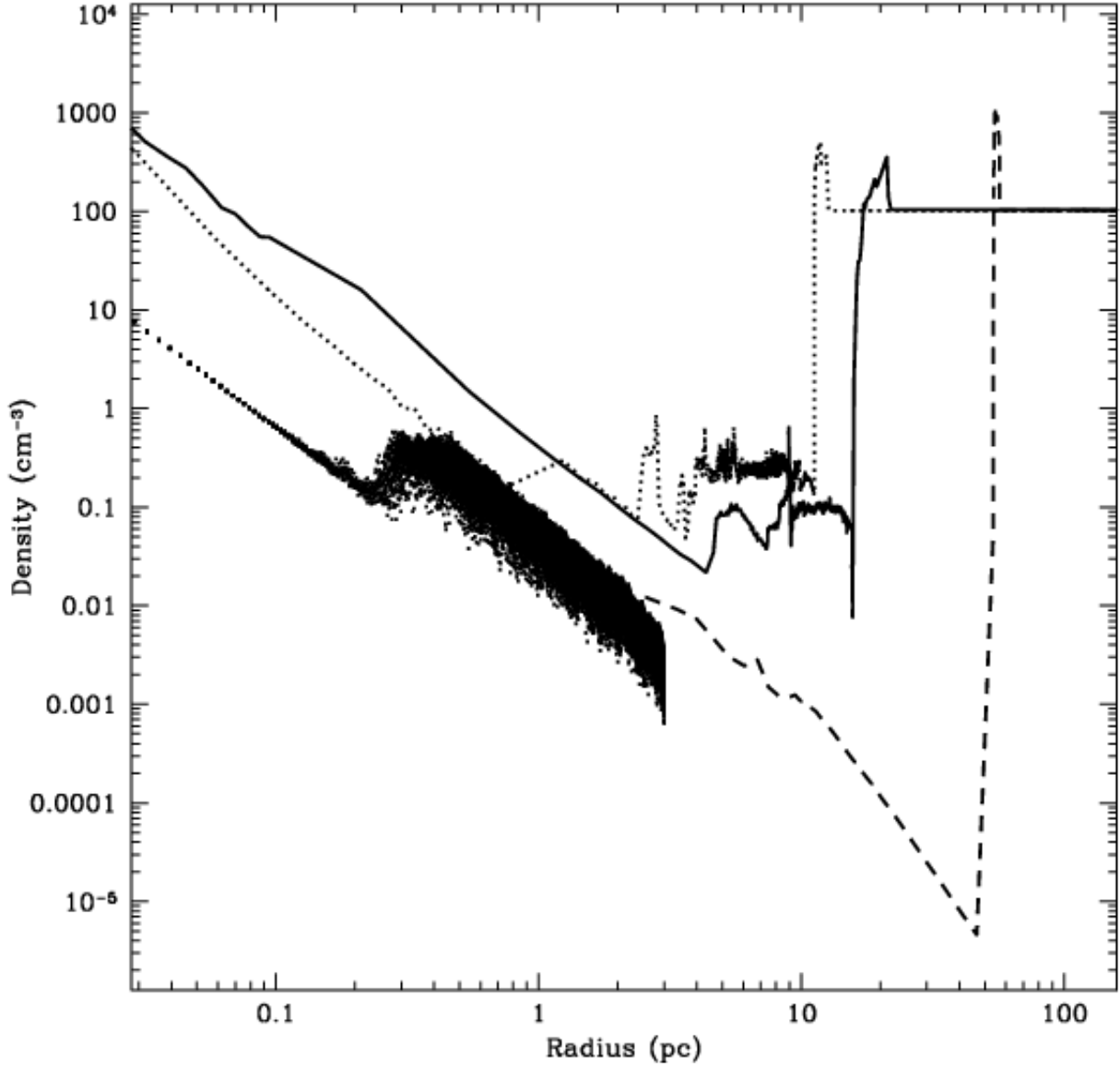


Fig. 3.— Density versus radius for the wind bubbles produced by our 3 stellar models: $40 M_{\odot}$ star (solid line), $23 M_{\odot}$ star (dotted), $16 M_{\odot}$ star (dashed line). The effects of the variable mass loss can be seen (for instance, see the density peak in the $23 M_{\odot}$ star at roughly 3 pc), but the density profiles still follow a roughly $\rho \propto r^{-2}$ profile even beyond the true termination shock of the free-streaming wind and far enough out that it should dominate what we see in the GRB afterglow observations. The points show the density profile along the z -axis in our 3-dimensional model. This model was for the $23 M_{\odot}$ binary star assuming zero density ambient medium except for a circumstellar disk caused by the binary interaction (see Fig. 4).

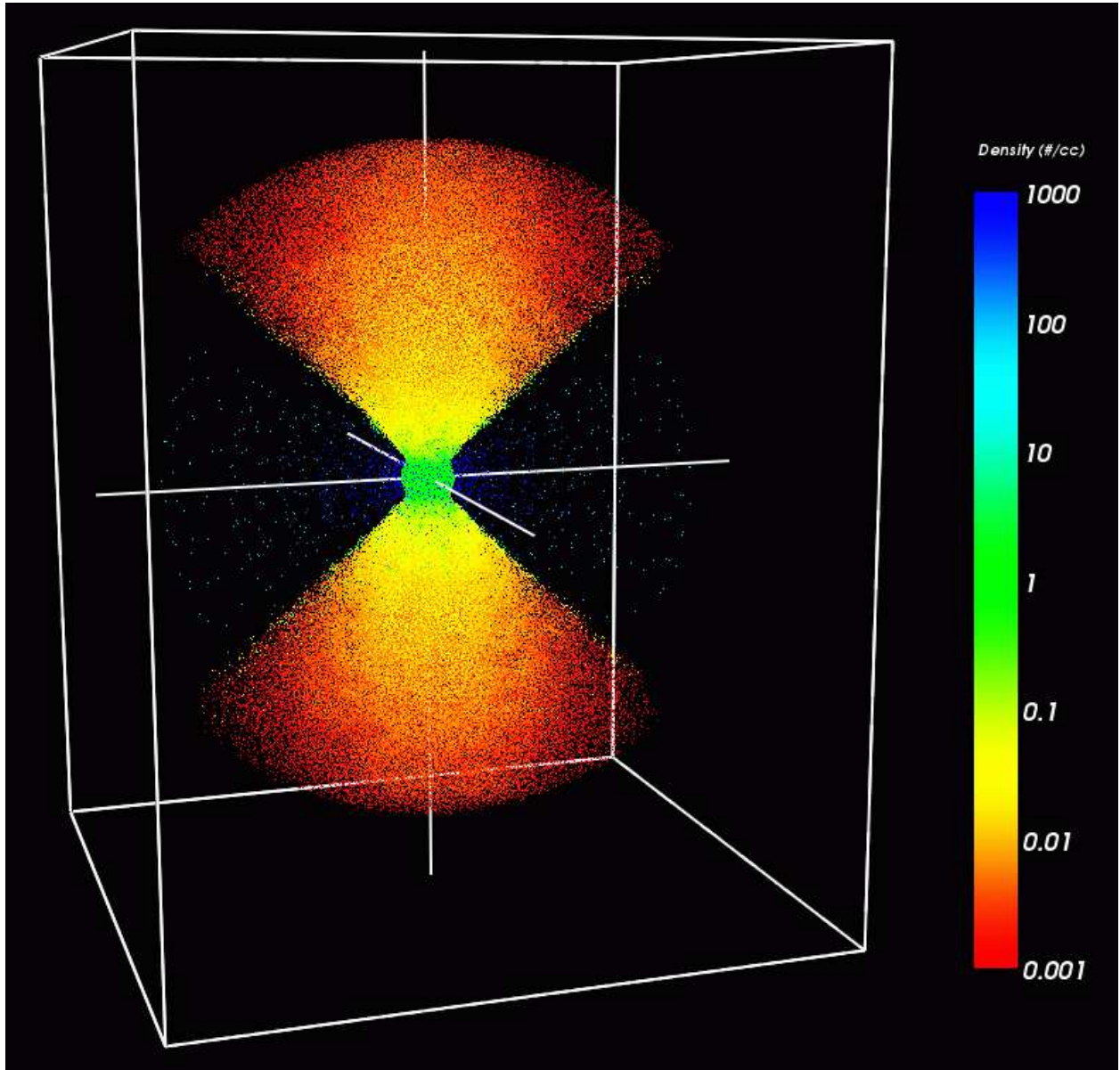


Fig. 4.— A 3-D SPH model of wind from a massive star interacting with a wedge of dense material ejected during the common envelope phase of a binary system. The location of each SPH particle is marked by a colored point, and the color indicates the number density of gas at that location. The wind-producing star is located at the center of the simulation box; the wedge of material ejected during the common envelope phase is oriented perpendicular to the z (vertical) axis. Wind particles are injected at a radius of 0.01 pc, the inner edge of the dense wedge is located at 0.3 pc, and particles are removed from the simulation when they travel more than 3 pc from the origin. The density of gas in the wedge is much larger than in the subsequently-ejected wind, so the wind is obstructed by the wedge and escapes primarily along the z axis.

Scenario I: Standard (CE evolution)

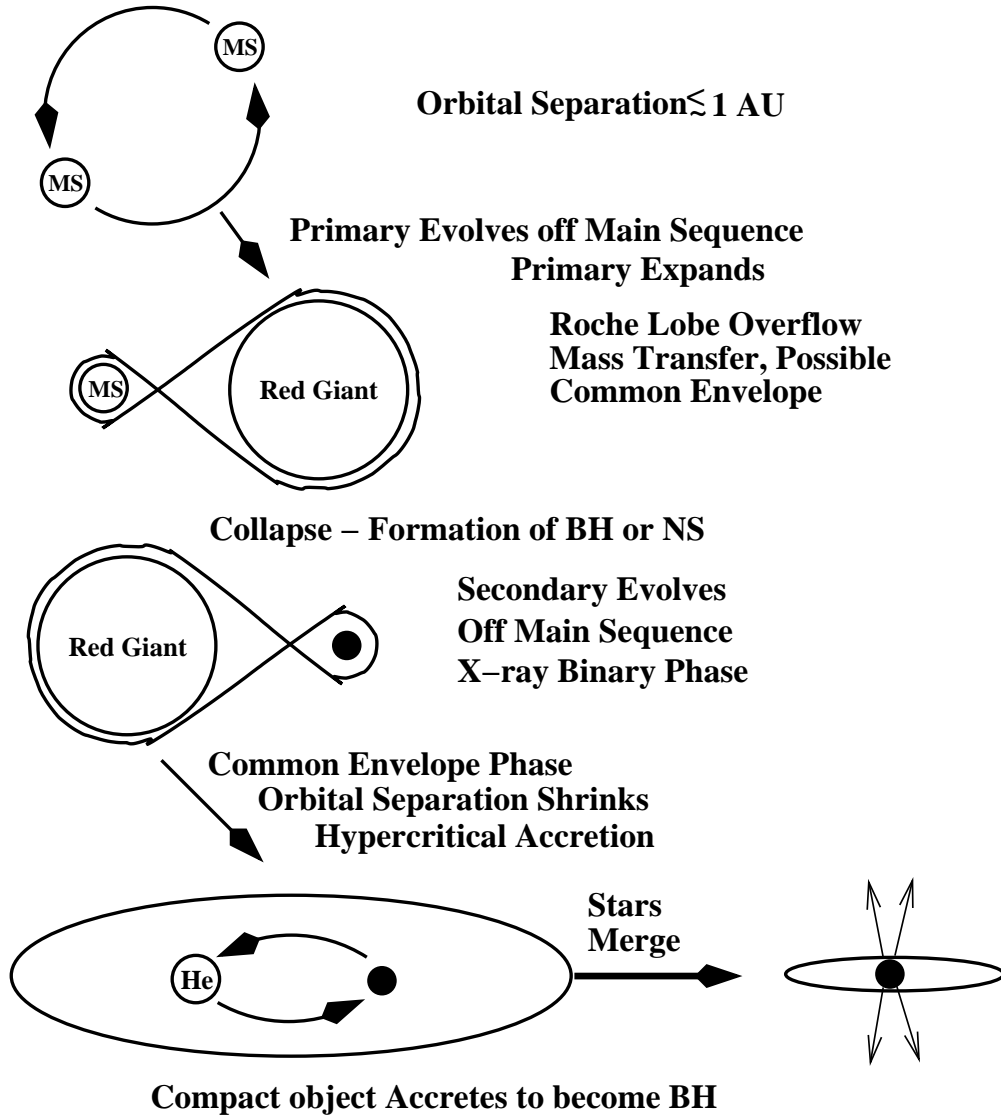


Fig. 5.— Standard formation scenario for He-merger progenitors. Two stars in a close binary undergo at least 1 common envelope phase, and often 2 such phases. The first, not required, occurs when the primary (more massive star) evolves off the main sequence. After the common envelope phase, the primary collapses to form a neutron star or black hole. If the system remains bound after this collapse and its orbit is close enough, the binary will go through a second common envelope phase when the companion to the compact remnant evolves off the main sequence. If the compact object merges with its companion, a Helium-merger is formed.

Scenario II: "Brown" Scenario

Initial Conditions:

$$M_P > M_{SN}$$

$$M_S \gtrsim 0.95 M_P$$

Orbital Separation $\lesssim 1$ AU

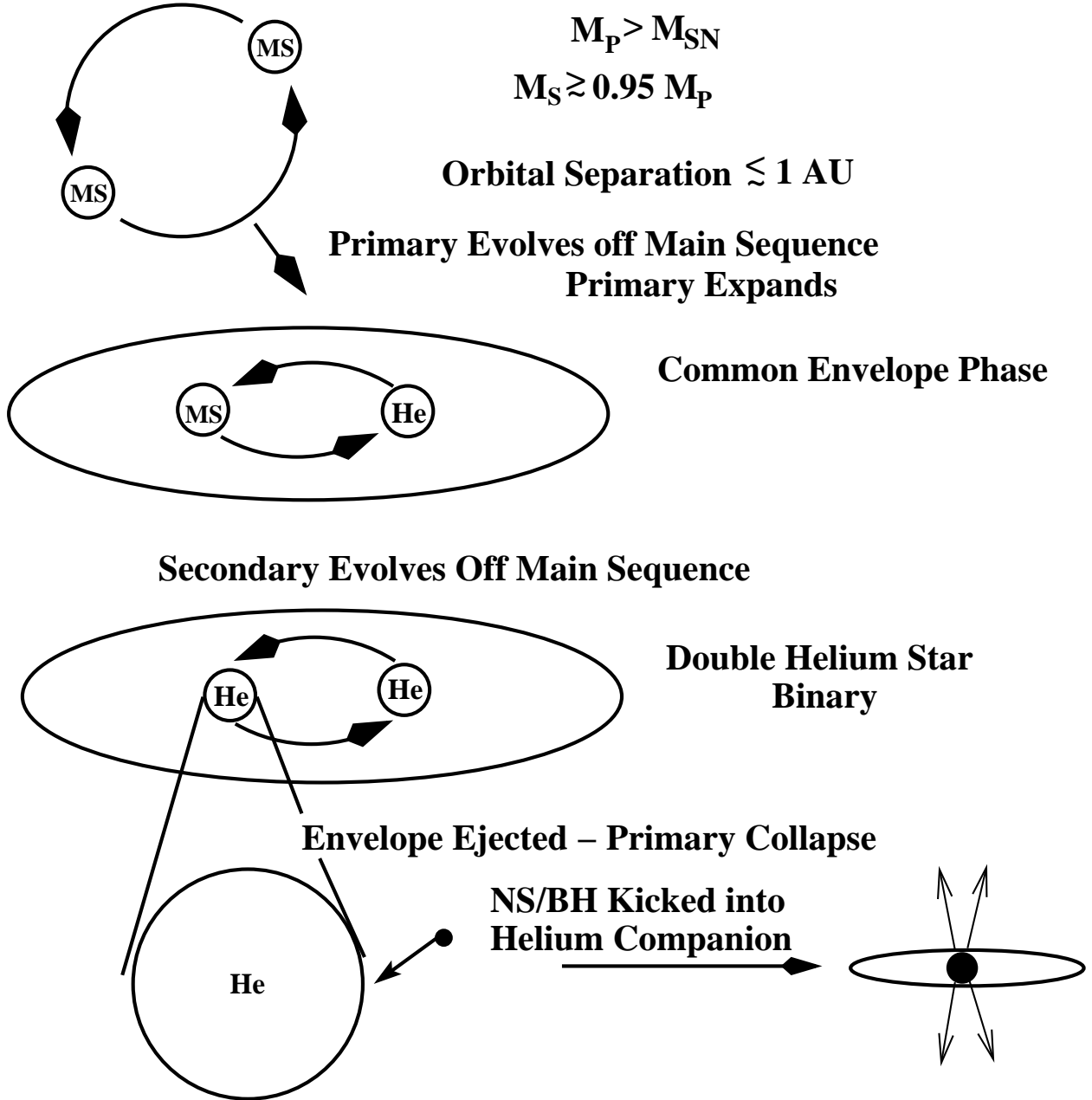


Fig. 6.— Secondary formation scenario of helium-mergers. Two nearly equal mass stars in a close binary evolve off the main sequence together - that is, the secondary evolves off the main sequence before the primary collapses. The “joint” common envelope phase from this evolution produces two helium stars. When one star collapses, its compact remnant may be kicked into the helium companion, producing a helium-merger.

Scenario III: Kick Progenitor

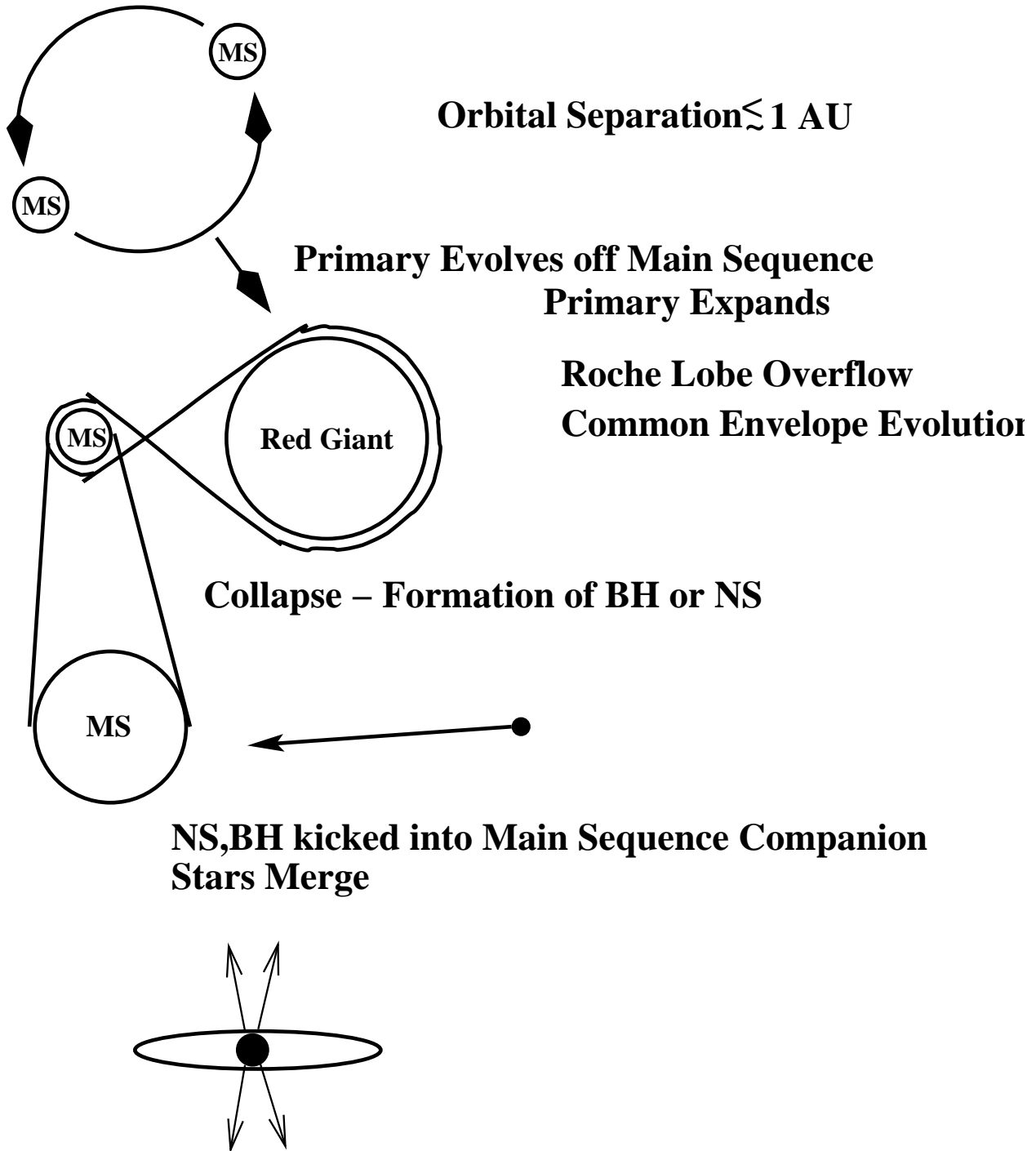


Fig. 7.— Alternate scenario for producing merged systems. In this close binary system, the collapse of the primary star kicks the compact remnant into its main-sequence companion. Although not strictly a Helium-merger because the companion is still on the main sequence (and hence not quite as dense and less likely to be an ideal GRB progenitor), we include it in our study.

Fig. 8.— A series of plots showing the population for all our He-merger formation scenarios (either total number or fraction) for our Standard model versus system velocity, merger time or distance travelled. The different curves denote different subclasses and have the same definitions for each plot: dark solid - all systems, dark dotted - angular momentum, light solid - BH Collapse, light dotted - NS Collapse, and dashed - Low-Wind (see Table 3 for details). a) Number of binaries per 1 km s^{-1} bin. The peak in low velocity systems only occurs in the neutron star compact object and small companion mass subclasses. The velocities are only high enough to escape the host galaxy gravitational potential if the host is an extremely low-mass galaxy. Note that the peak in low-velocity systems is dominated by the NS Collapse and Low-Wind models. It is difficult for those systems that form neutron stars to remain bound, requiring the kick to counter the momentum lost in the supernova ejecta. The systems that are more likely to remain bound for these NS binaries are those where the countering effects lead to small proper motions. b) Number of binaries per log Time bin (900 bins in plot). The large spike in binaries with merger times $\lesssim 10\text{y}$ arises from the Brown and MS Merger formation scenarios. These scenarios only produce immediate mergers. The bulk of long merger times are produced by those mergers with low wind (and hence low-mass) companions. c) Number of binaries per 1 pc bin. The spike at low distances corresponds to the Brown and MS-merger formation scenarios where the merger time is nearly immediate (see figure 8b). Even for the primary He-merger scenario, most mergers occur within 100 pc of their formation site. A small fraction occur beyond 1 kpc (Table 6). d-f) Same as figures a-c) but showing the relative fractional distribution (Number in a bin divided by the total number of a given subclass).

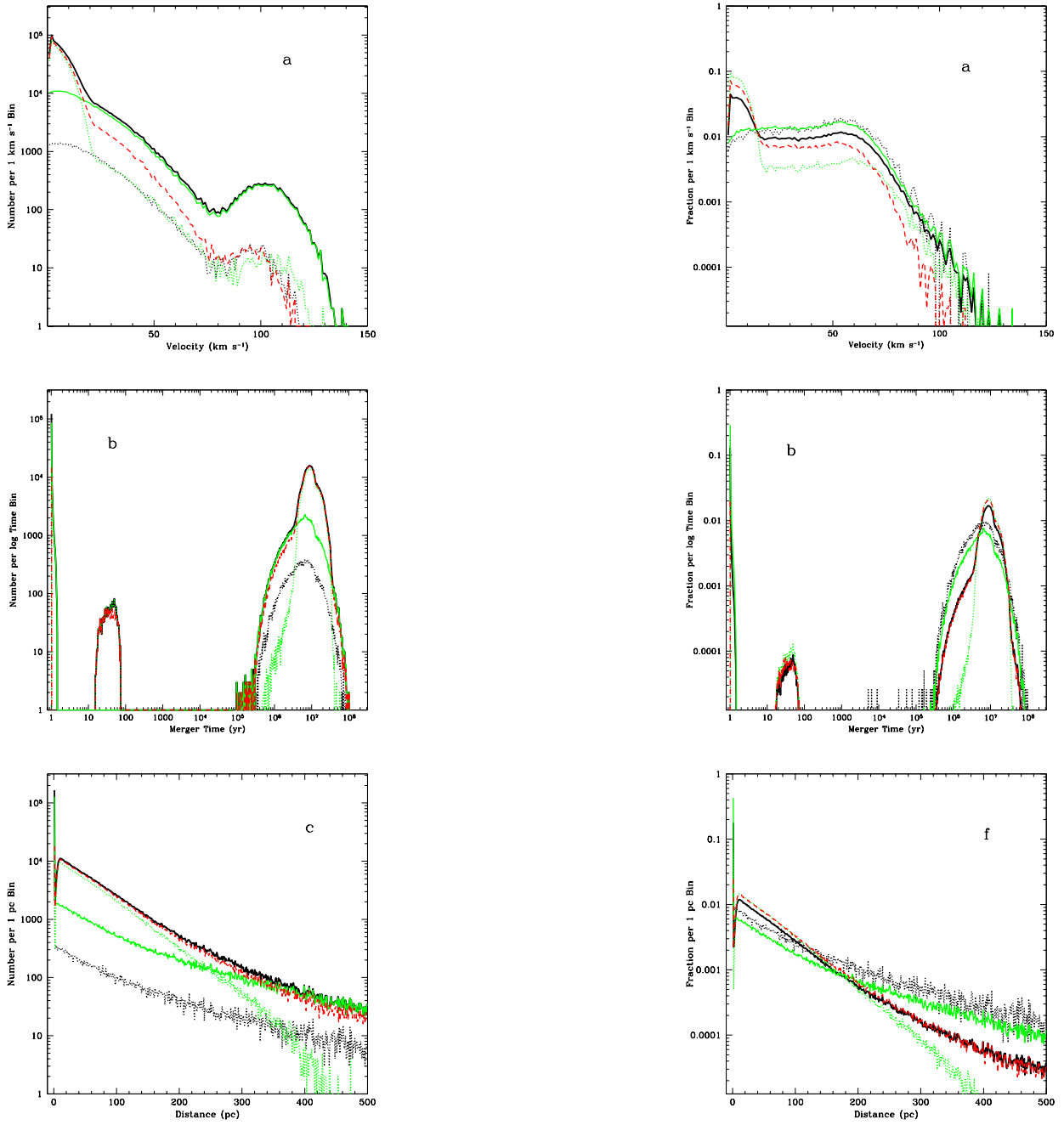


Fig. 8. —

Fig. 9.— Relative fractional distributions for model Max300. These 3 figures are identical in scale to figures 8d-f and can be compared directly to the results of the standard model in figure 8. Note that because the kick in this model is single-peaked, the double peak in the velocity distribution does not occur in this model.

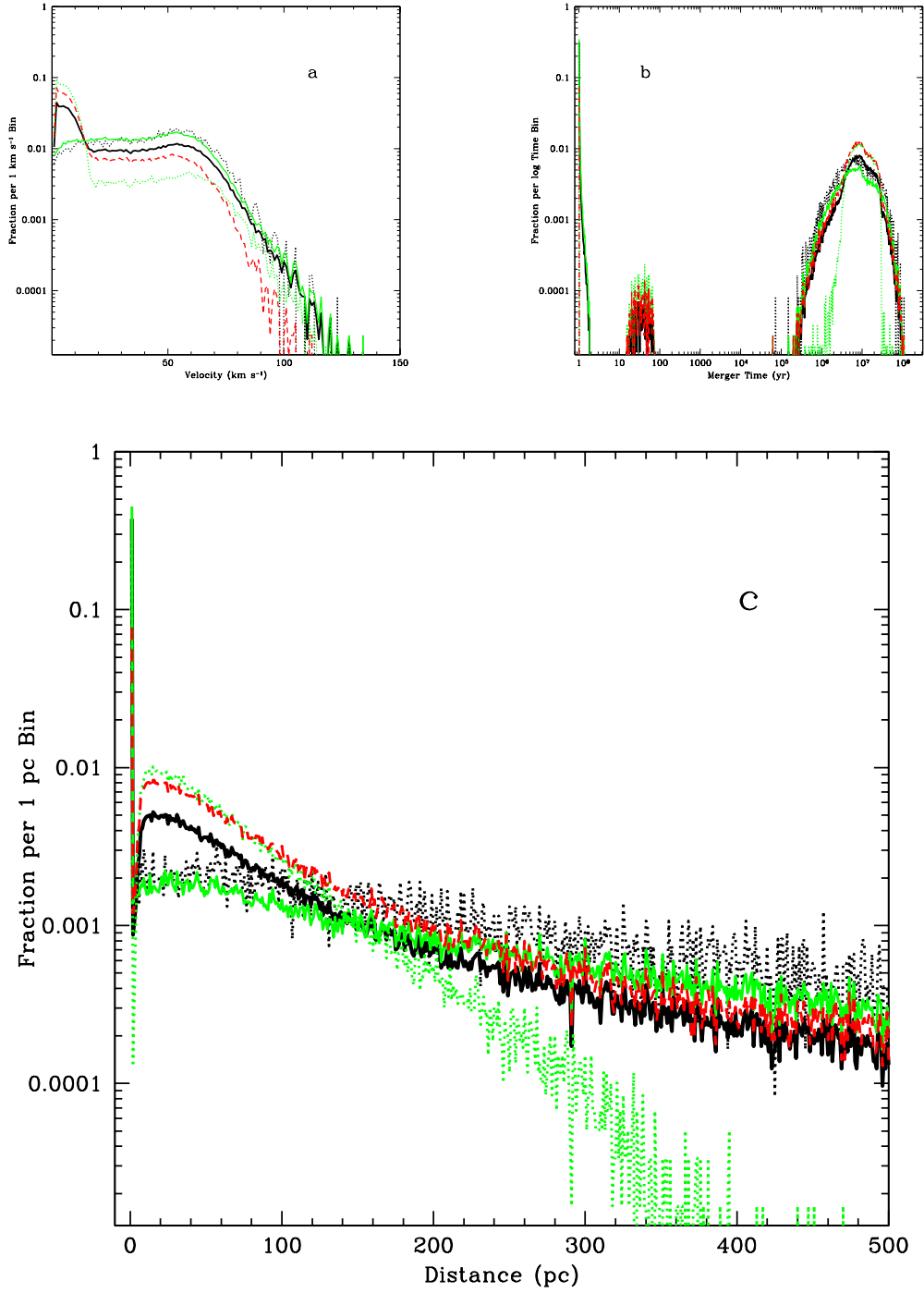


Fig. 9. —

Fig. 10.— Same as Figure 9 showing just the total He-merger distributions for a range of population synthesis progenitors: black solid (Standard), red solid (FBBLowRad), red dotted (FBBHighWind), green solid (StanCE1.0), green dotted (StanCE0.2), blue solid (IMF2.7MT1.0), blue dotted (IMF2.7CE0.2), cyan solid (IMF2.7CE0.5). The largest variations are caused by those models where the stellar radii or stellar mass loss was modified.

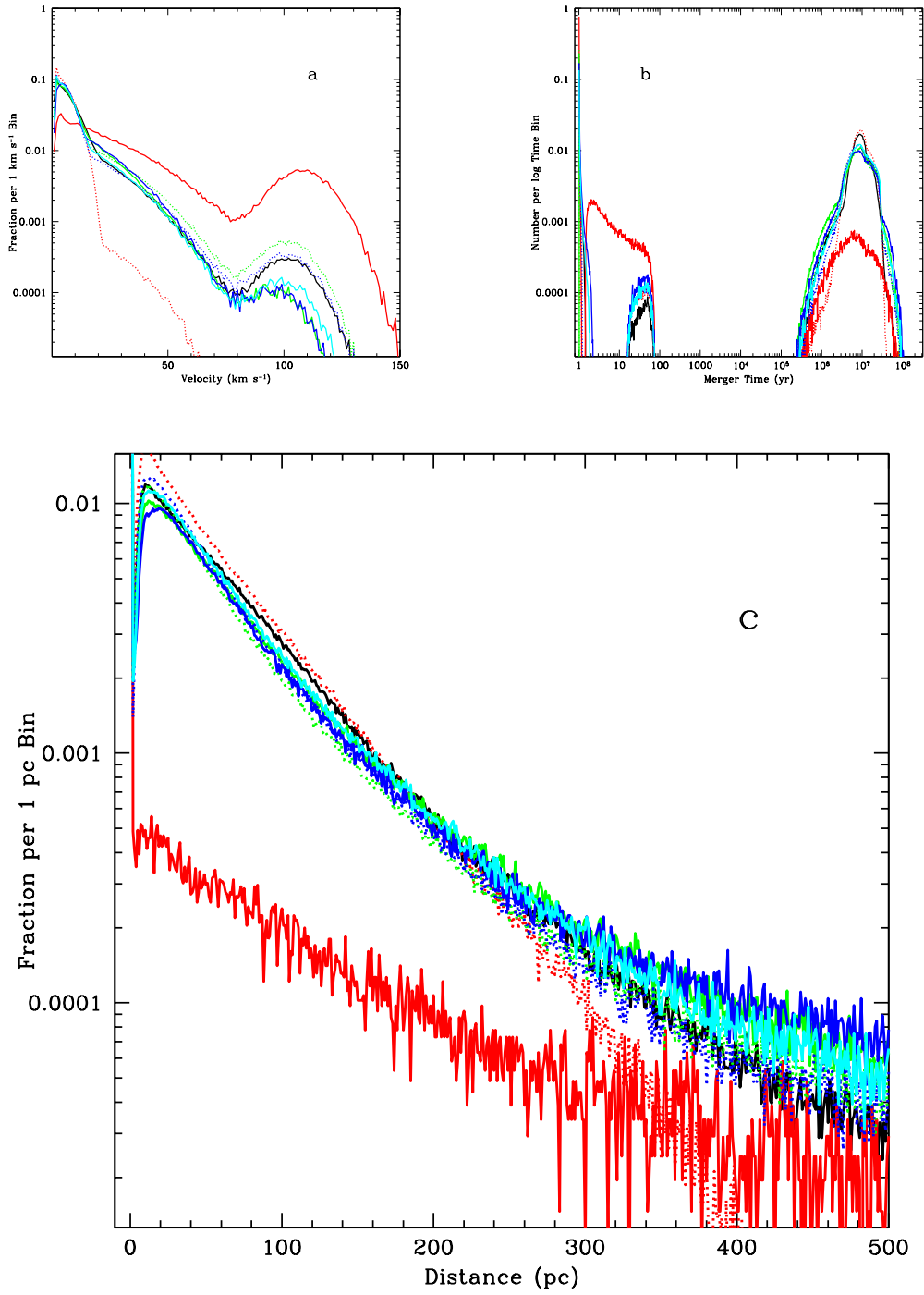


Fig. 10. —

Fig. 11.— Same as Figure 9 showing just the total He-merger distributions as a function of kick magnitude (using single peaked maxwellian distributions): blue solid (Max100), cyan solid (MAX150), green solid (MAX200), blue dotted (MAX300), cyan dotted (MAX400), green dotted (MAX500), red dotted (MAX300IMF). Note that the kick distribution has a much larger effect than changes in the initial mass function.

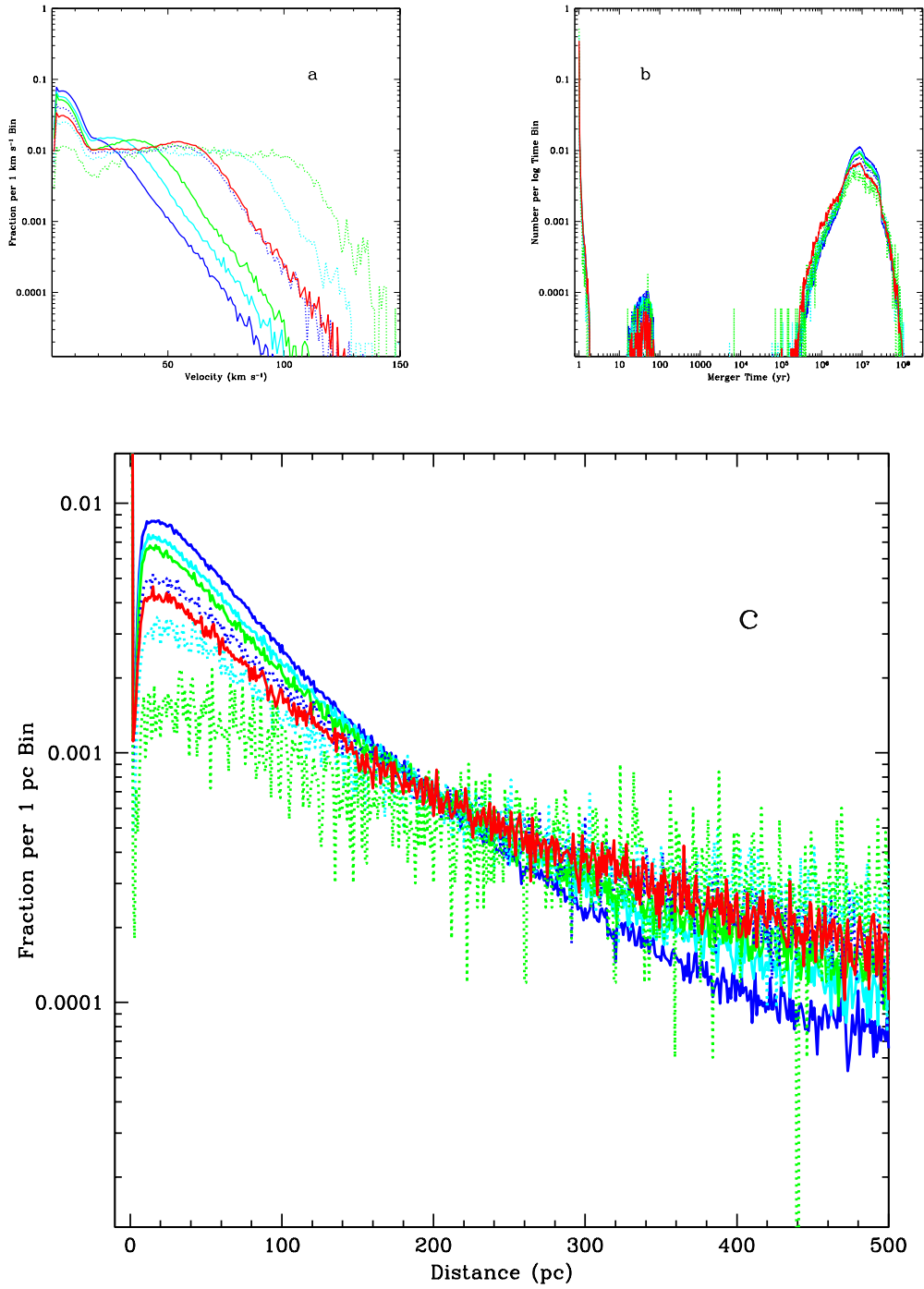


Fig. 11. —